UNIVERSITY OF OKLAHOMA

GRADUATE COLLEGE

THE STRATIFORM RADIATION EFFECT ON TROPICAL ORGANIZED DEEP CONVECTION

A THESIS

SUBMITTED TO THE GRADUATE FACULTY

in partial fulfillment of the requirements for the

Degree of

MASTER OF SCIENCE

By

EMILY LUSCHEN

Norman, Oklahoma

2023

Downloaded from SHAREOK. Persistent Handle URL: https://hdl.handle.net/11244/339848

THE STRATIFORM RADIATION EFFECT ON TROPICAL ORGANIZED DEEP CONVECTION

A THESIS APPROVED FOR THE
SCHOOL OF METEOROLOGY

BY THE COMMITTEE CONSISTING OF

Dr. James Ruppert, Chair
Dr. Naoko Sakaeda
Dr. Greg McFarquhar

© Copyright by EMILY LUSCHEN 2023
All Rights Reserved.

Acknowledgements

I would like to first thank my advisor Dr. James Ruppert for his guidance these past two years. I would also like to thank my committee members for their input and time spent reading this thesis. I also thank Dr. Shun-Nan Wu and Dr. Yunji Zhang for their help in the creation of this product, especially early on in its development. I would like to acknowledge Dr. Rosimar Rios-Berrios for her code that helped contribute to the creation and analysis within this thesis. Furthermore, I appreciate NSF for funding (AGS1712290) some of my travel in the past two years as well as for funding me the next three to five years. I of course must acknowledge my friends and officemates of the last two years. Thank you for keeping me sane. Finally, I want to thank my parents and my family for their part in helping me achieve my dreams.

Table of Contents

Acknowledgements iv
List of Tables vi
List of Figures vii
Abstract viii
1 Introduction 1
2 Data and Methods 6
2.1 Numerical Model Simulations 6
2.2 Precipitation Classification 7
2.2.1 Description and Development 8
2.2.2 Comparison and Validation 12
3 Longwave Radiative Feedback as a Function of Cloud Mode 17
3.1 Atmospheric Cloud Radiative Effect (ACRE) and Cloud Radiative Forcing (CRF) 17
3.2 Moist Static Energy Variance 20
4 The Stratiform Radiation Effect in a TC Context 24
4.1 Development of Haiyan 25
4.1.1 Evolution of Cloud Fraction 25
4.1.2 Midlevel Vortex Intensification 29
4.2 Impacts of Stratiform CRF on Dynamical Mechanisms Promoting TC Genesis 32
4.2.1 Stratiform CRF Weakens Downward Vertical Mass Flux (VMF) 32
4.2.2 Stratiform CRF and an Increase in Positive Buoyancy 35
4.2.3 Stratiform CRF and a Moister Storm Column 36
5 Summary and Conclusions 39
6 Reference List 42

List of Tables

Table 2.1: Comparison of cloud type domain fraction between the new classification (deep convective, congestus, shallow convection, anvil) and the traditional classification (convective, stratiform, and anvil). Table contains values for the first member of Haiyan CTL at the timestep 36 hours. 12

List of Figures

Figure 1.1: (a) Idealized net heating profiles of stratiform and convective precipitation regions in a mesoscale convective system. (b) Net heating profiles based on varying percentages of stratiform within a mesoscale convective system. From Houze (2004).....5

Figure 2.1: Flow chart summarizing the categorization process for our precipitation classification algorithm.....10

Figure 2.2: TWP frequency for the traditional classification. The convective mode is in blue, the stratiform mode is in red, and the anvil mode is in black. The vertical black line indicates the TWP threshold for our algorithm. Figure shows the first member of Haiyan CTL at the timestep 36 hours.....11

Figure 2.3: The CR frequency for the traditional classification. The convective mode is in blue, the stratiform mode is in red, and the anvil mode is in black. The vertical black line indicates the CR threshold for our algorithm. Figure shows the first member of Haiyan CTL at the timestep 36 hours.....11

Figure 2.4: Maps comparing a) microphysics-based classification scheme, the b) traditional reflectivity classification, c) 1000 hPa rain mixing ratio. Colors indicate non-raining (white), deep convection (a; teal), convection (b; teal), congestus (a; pink), shallow convection (a; orange), stratiform (yellow), and anvil (blue). All panels show the first member of Haiyan CTL at the timestep 36 hours.....13

Figure 2.5: Maps depicting precipitation classification for the first five members using the new microphysics-based classification. All panels show Haiyan CTL at 36 hours. 13

Figure 2.6: Vertical motion (w) profiles of a) convective and b) stratiform regions. The microphysics classification is broken into deep convective (a; teal), congestus (a; pink), shallow convective (a; orange), stratiform (b; solid yellow), and anvil (b; solid blue). The profile of all convective types from the microphysics classification is in dashed black. The traditional classification w profiles are categorized into convective (a; solid black), stratiform (b; dashed yellow), and anvil (b; dashed blue). Both panels show the first member of Haiyan CTL at the timestep 36 hours.....15

Figure 3.1: Boxplots of domain averaged LW ACRE by precipitation type. White circles indicate the mean value. Black diamonds represent outliers. Plots include values from all 10 members and 85 timesteps for Haiyan CTL. 18
Figure 3.2: Maps showing the ACRE for a) convective categories, b) stratiform and anvil, and c) all categories. The legend contains the domain-averaged ACRE for the respective precipitation categories. All panels show the first member of Haiyan CTL at 36 hours. 18
Figure 3.3: As in **Figure 3.1** but for class averaged LW ACRE. 19
Figure 3.4: CRF vertical profiles of a) convective and b) stratiform/anvil regions. The microphysics classification is broken into deep convective (a; teal), congestus (a; pink), shallow convective (a; orange), stratiform (b; yellow), and anvil (b; blue). The averaged convective and stratiform/anvil profiles are in dashed black in a) and b). The convective (red) and stratiform/anvil (blue) are repeated in the third panel (c) for comparison. 20
Figure 3.5: As in **Figure 3.1** but for LW MSE variance. 22
Figure 3.6: As in **Figure 3.3** but for LW MSE variance. 22
Figure 3.7: As in **Figure 3.2** but for LW MSE variance. 23
Figure 4.1: Tracks for all 10 ensemble members following a 600-hPa absolute vorticity maximum in the CTL Haiyan simulation. Member 10 is in light purple. 25
Figure 4.2: Cloud fraction for 9 members of CTL Haiyan. The solid line indicates the hourly average across members. Shading indicates 95% confidence intervals. Categories include deep convective (teal), congestus (pink), shallow convective (orange), stratiform (gold), and anvil (blue). Area fractions are calculated within a 600 km radius around the domain 600 hPa vorticity maximum. 26
Figure 4.3: Timeseries of a 9-member average of the maximum 850 hPa wind within a 600 km radius of the 600 hPa midlevel vortex for Haiyan. Lines indicate the mean for CTL (black) and NCRF (red) tests. Shading represents the 95% confidence interval. 27
Figure 4.4: Cloud fraction hourly means for 9 members for Haiyan tests CTL (black), NCRF (red), C-NCRF (green), SA-NCRF (blue), and S-NCRF (yellow). Cloud types include a) deep convective, b) congestus, c) shallow convective, d) stratiform, and e) anvil. Area fractions are calculated within a 600 km radius around the domain 600 hPa vorticity maximum. 28

Figure 4.5: Time series of a 9-member average of the maximum 850 hPa wind within a 600 km radius of the 600 hPa midlevel vortex for Haiyan. Lines indicate the mean for CTL (black), NCRF (red), SA-NCRF (blue), C-NCRF (dashed green), and S-NCRF (yellow).....29
Figure 4.6: As in **Figure 4.3** but for 600 hPa absolute vorticity. 30
Figure 4.7: As in **Figure 4.5** but for 600 hPa absolute vorticity. 31
Figure 4.8: Contoured frequency by altitude diagrams (CFADs) of the difference in vertical mass flux (VMF) between CTL and a) NCRF ; b) C-NCRF ; c) SA-NCRF ; and d) S-NCRF one hour after the start of the sensitivity tests. Red shading indicates CTL has a greater frequency and blue shading indicates the sensitivity test has a greater frequency. Mean profiles to the left show the mean difference between the tests. 33
Figure 4.9: Same as **Figure 4.8** but for 6 hours after the start of the sensitivity tests. 34
Figure 4.10: Same as **Figure 4.9** but for anomalous virtual potential temperature $\theta v'$. 36
Figure 4.11: Same as **Figure 4.9** but for Lvq' 37

Abstract

Idealized studies of self-aggregation have implicated the importance of longwave (LW) cloud-radiative forcing (CRF) in facilitating the upscale development of moist convection. While different cloud structures are known to have distinct CRF, the relative role of distinct cloud and precipitation types in driving upscale development through radiative feedback is largely unexplored. Considering the impact CRF has on convection, we hypothesize that different cloud modes have different effects on mesoscale tropical convection through radiative feedback. We test this hypothesis by analyzing output from Weather Research and Forecasting (WRF) model simulations of Super Typhoon Haiyan. Using a novel column-by-column precipitation classification scheme, we use this model output to identify the relative contribution of 5 cloud types to the direct LW radiative forcing and the upscale development of convection via LW moist static energy variance. Results indicate that stratiform and anvil regions contribute dominantly to the domain averages of these variables.

We next compared the control simulation (CTL) to sensitivity tests that exclude cloud-radiative feedback (NCRF) either everywhere or only in specific cloud types. These tests indicate that the upscale development of deep convection that manifests in tropical cyclone (TC) genesis is accelerated by CRF, especially of that in stratiform regions. There is a growing consensus from observations that the areal growth of stratiform precipitation is a key precursor to TC genesis and intensification. This observational finding presents a conundrum, given that stratiform precipitation is directly tied to downdrafts, and hence ventilation. Therefore, we hypothesize that the cloud-radiative effect within stratiform cloud regions weakens downdrafts, allowing the environment to moisten more easily. Analysis shows that CTL tests have less downward vertical mass flux in the mid to lower troposphere, indicating weaker (and/or fewer) downdrafts, than that of the NCRF tests, with the greatest differences being in stratiform regions. These findings support our hypothesis that cloud-radiative effects in the stratiform regions weaken downdrafts in developing TCs, in turn allowing the environment to moisten more easily. Understanding the importance of cloud type CRF, especially that of stratiform, could provide insight on the development of tropical convection and TC genesis.

1 Introduction

Clouds are often viewed as simply a marker of moist convection ("convection" hereafter) or turbulence due to the nature of their formation. However, clouds are not just a byproduct of their formative circulation. They can also modify their regional climate, which further impacts the global system, through their feedback with longwave (LW) and shortwave (SW) radiation (Bony et al. 2015; Voigt et al. 2021). This feedback influences the warming and cooling of local temperatures. For example, one component of LW cloud-radiative forcing (CRF) acts as a greenhouse effect where clouds trap Earth's outgoing LW radiation and emit it back downward. As a result, the mid- to lower troposphere experiences more heating. Over the past few decades, we have gained a better understanding of climate sensitivity and how cloud feedbacks affect it (Zelinka et al. 2020). But there are still questions related to how cloud feedbacks and CRF impact convection (Bony et al. 2015). Recently, some studies have begun to highlight the importance of CRF in the dynamics of tropical convection (e.g., Bretherton et al. 2005; Wing et al. 2016; Ruppert et al. 2020; Najarian and Sakaeda 2023), yet there have been limited studies on the impact of different cloud types' contribution to CRF and the resulting effect on mesoscale convective evolution.

Studies on self-aggregation, or the spontaneous initiation and clustering of convection, have sparked our understanding of the significance of CRF in triggering the upscale development of tropical convection. Self-aggregation develops in idealized model frameworks in radiative-convective equilibrium (RCE), or when radiative cooling is balanced with convective heating, which is an approximation for the real tropical atmosphere (Manabe and Strickler 1964; Bretherton et al. 2005). Through mechanism-denial experiments it was found that self-aggregation in non-rotating simulations does not occur without the presence of the LW radiation through CRF (Muller and Held 2012; Wing and Cronin 2016). The only way for self-aggregation to develop in a non-rotating framework without the LW feedback is when evaporative-driven downdrafts and cold pools are artificially weakened, keeping moisture localized to convective regions (Muller and Bony 2015). Despite the idealized nature of RCE model frameworks, these studies suggest the important role CRF may play in the upscale development of tropical convection.

There are two ways to quantitively evaluate self-aggregation. The first is through the variance of precipitable water (PW). During self-aggregation, areas that have suppressed deep convection become drier while regions of enhanced convection increase in moisture (Wing et al.

2017). However, domain averaged PW is not a conserved quantity, decreases with aggregation, and is sensitive to sea surface temperature (SST; Wing et al. 2017a). So, Wing and Emanuel (2014) developed another metric to quantify self-aggregation through column-integrated moist static energy (MSE). They derived a budget for frozen MSE, MSE associated with frozen hydrometeors, based on its horizontal variance. As convection in the model domain aggregates, the MSE variance between convective and non-convective regions grows as MSE variance is dominated by moisture variations (Wing and Emanuel 2014). Although MSE changes with SST, the horizontal variance of MSE across simulations is similar (Wing et al. 2017). The variance budget consists of four source terms: surface fluxes, SW radiation, LW radiation, and advection (Wing and Emanuel 2014). While all are important for the generation of self-aggregation, not all are required for maintenance of the convective cluster (Wing et al. 2017). It is the LW radiation term and its interaction with clouds that dominates and maintains a mature cluster (Wing and Emanuel 2014; Wing and Cronin 2016).

Adding a rotating framework to RCE provides insight for tropical cyclones. When self-aggregation studies are run including the Coriolis effect, tropical cyclogenesis occurs (Bretherton et al. 2005; Wing et al. 2016). Like non-rotating frameworks, the LW radiative feedback considerably aids the development of self-aggregation, but differing from non-rotating frameworks in that it is not required due to stronger surface flux feedback from the addition of rotation (Wing et al. 2016). Although rotating RCE studies can help spark new understanding for how tropical cyclones form, caution is required when applying to the real atmosphere, given the idealizations of the RCE framework. There have been relatively limited studies that test the role of LW radiation cloud feedback in tropical convection in more realistic environments. Ruppert et al. (2020) evaluated the role of LW radiation feedbacks in Weather Research and Forecasting (WRF) model simulations with the generation of Super Typhoon Haiyan (2013) and Hurricane Maria (2017) to find that including CRF accelerated tropical cyclone development. Another study by Wu et al. (2021) noted that homogenizing the LW heating rates across the domain of a WRF simulation inhibited the generation of tropical cyclones. These studies have confirmed the importance of LW radiation cloud feedback for tropical cyclone genesis, but there is still much left to be understood on how and through what mechanisms LW radiation accelerates convective upscale development and TC development.

CRF is almost always a requirement for self-aggregation and likely an important aspect for initiating and maintaining convective organization in the tropics. The LW radiative effect works to increase moisture in already moist areas (Bretherton et al. 2005). The column-integrated CRF, or atmospheric cloud-radiative effects (ACRE), prompts a thermally direct circulation that transports moisture against the gradient into already moist regions (Needham and Randall 2021a,b). It is no surprise that a moister tropical environment would result in an increase in precipitation rates, but what is compelling is the nonlinear relationship found between the two (Bretherton et al. 2004). Ahmed and Schumacher (2015) concluded that this nonlinear relationship between relative humidity and precipitation rates in the tropics is a consequence of the nonlinear growth of stratiform rainfall coverage with relative humidity. In this same way, ACRE can also be related to relative humidity, as ACRE's strength is related to stratiform cloud coverage (Needham and Randall 2021a). Due to the larger areal coverage of stratiform regions compared to that of convective regions, ACRE tends to be greater in stratiform regions (Needham and Randall 2021a). Following that CRF is likely important for the initiation and maintenance of tropical convection, we hypothesize that stratiform CRF, specifically, supports convective organization through stratiform's dominant role in ACRE which relates to the MSE feedback.

There has been limited research characterizing the LW radiative profiles of different cloud types. One observational study has looked at the SW and LW heating profiles of anvil clouds in the tropics (Wall et al. 2020). A recent study by Najarian and Sakaeda (2023) determined the cloud-radiative heating profiles for the Madden Julian Oscillation (MJO) for different cloud types using observations. The results showed unique heating profiles for each cloud mode and emphasized the deep warm layers created by anvil and deep convective regions. Understanding the distinct nature and role of radiative heating in different cloud types is important for a complete understanding of tropical convection. This understanding will better enable us to validate and improve numerical models where necessary. Considering the limited number of studies that quantify LW radiative heating and feedback as a function of different precipitating cloud ("cloud" hereafter) types and with no studies examining the LW MSE variance term by cloud type, we list our first science objective for this thesis.

SO 1: Determine the LW CRF profiles and MSE variance source term contributions of different cloud types via the development of an expanded column-by-column classification scheme based on microphysical cloud and precipitation properties.

Understanding the individual contribution of different cloud types to LW CRF is not only useful for studying general tropical convection but can also contribute to our understanding of TC development. Most of the literature on TC genesis and intensification emphasizes the role of deep convective regions (e.g., Hendricks et al. 2004; Montgomery and Smith 2017; Bell and Montgomery 2019). But observation-based studies indicate that the areal growth of stratiform precipitation regions is a key precursor to TC intensification. One such study discovered that TCs undergoing a rapid intensification (RI) event experience a greater increase in stratiform rainfall coverage hours before the RI event begins (Tao et al. 2017). Overall, stronger TCs tend to have larger stratiform coverage, especially as they mature (Yokoyama and Takayabu 2008). This relationship between stratiform coverage and intensification is peculiar, as stratiform regions are linked to a column drying mechanism.

TCs require mid-level moisture for TC genesis and intensification to occur (Bister and Emanuel 1997; Gray 1998; Tang and Emanuel 2012), so it is odd that stratiform regions would expand prior to intensification relative to deep convection. The latent heating and divergence profiles of convective and stratiform regions are found in **Figure 1.1**. By approximating the latent heating rates to vertical motion to the first order, stratiform regions produce downdrafts in the low-levels and updrafts in the upper-levels. Together, this creates convergence in the mid-levels. This convergence transports dry, low moist entropy air into the column from the surroundings, which is detrimental to the development of the TC (Tang and Emanuel 2010). As Bister and Emanuel (1997) noted, the negative drying effects of downdrafts need to be lessened for tropical cyclogenesis to occur. Rios-Berrios (2020) found through idealized simulations that including radiation can decrease the strength of downdrafts by weakening cold pools but did not isolate the role of CRF. Given this finding, we hypothesize that CRF, specifically in stratiform regions, promotes and accelerates TC genesis by weakening stratiform downdrafts and, thus, increasing moisture and MSE in the storm column. Therefore, this thesis will investigate the following additional science objectives:

SO 2: Identify the relative importance of CRF on TC genesis and development as a function of distinct precipitating cloud types.

SO 3: Examine how stratiform CRF works to promote and accelerate TC genesis.

This thesis is further divided into four chapters. The second chapter contains a description of the data and methods with a section devoted to the precipitation classification algorithm mentioned in **SO 1**. Chapter 3 summarizes and discusses the results for **SO 1** while Chapter 4 focuses on **SO 2** and **SO 3**. Chapter 5 summarizes and concludes our findings.

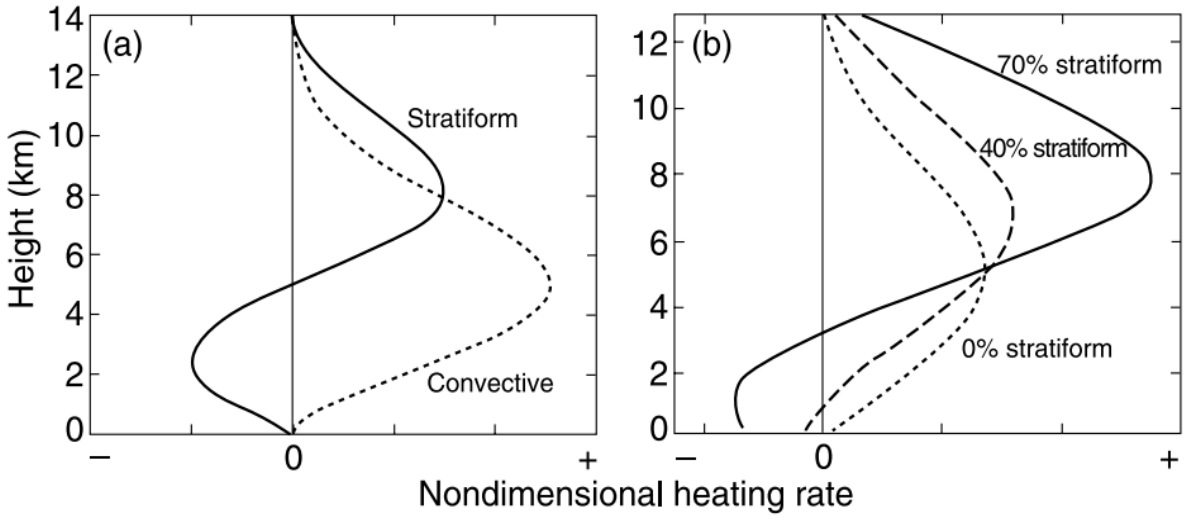

Figure 1.1: (a) Idealized net heating profiles of stratiform and convective precipitation regions in a mesoscale convective system. (b) Net heating profiles based on varying percentages of stratiform within a mesoscale convective system. From Houze (2004).

2 Data and Methods

2.1 Numerical Model Simulations

To quantify the role of different precipitation types on CRF and their subsequent impact on tropical convection, we recreate two notable TCs for this study: Super Typhoon Haiyan (2013) and Hurricane Maria (2017). Both were chosen based on their high intensity and because they developed in typical environments for tropical cyclogenesis, including weak vertical wind shear and above average sea surface temperatures (SSTs; Ruppert et al. 2020). These two cases are therefore taken to represent a larger population of TC cases.

The simulations for this study consist of a 10-member ensemble for each storm using the Advanced Research Weather and Forecasting model (WRF-ARW, version 4.3.1; Skamarock et al. 2008). We use a nested domain with the outer domain's initial and boundary conditions initiated from the first 10 ensemble members of the NOAA-NCEP Global Ensemble Forecast System (2015) retrieved from the NOAA National Centers for Environmental Information. The model is run with 55 vertical levels and a horizontal grid spacing of 9 km in the outer domain and 3 km in the inner domain. The microphysics is represented by Thompson and Eidhammer's (2014) two-moment scheme.

The control simulations (CTL) for Super Typhoon Haiyan and Hurricane Maria were integrated from 0000 UTC 1-0000 UTC 5 November 2013 and 1200 UTC 14-1200 UTC 20 September 2017, respectively. The CTL simulation ran for a total of 96 hours based on computational limitations. The CTL simulations have clouds interacting with radiation as in nature using the SW and LW radiation schemes from the Rapid Radiative Transfer Model for GCMs (RRTMG; Iacono et al. 2008), which is fully coupled to the microphysics scheme. We also conduct sensitivity tests (NCRF), which have clouds that are transparent to radiation to suppress the CRF. Clouds are made transparent to radiation by omitting hydrometeors from the radiation flux calculations, leaving only those interactions with gaseous elements. To separately test the impact CRF has from bulk convective and stratiform/anvil regions, we ran additional sensitivity tests for Haiyan that selectively suppress the CRF in convective regions (C-NCRF) and in both the stratiform and anvil regions (SA-NCRF). We conducted a final test in which CRF was repressed in stratiform regions only (S-NCRF) to further distinguish the influence of stratiform CRF from anvil

CRF. The NCRF test restarts from CTL at 48 h for Maria and all NCRF tests for Haiyan restart at 36 h. The focus of the work presented in this thesis is on Haiyan.

2.2 Precipitation Classification

To carry out the sensitivity tests listed above, we must use an algorithm that can properly separate the cloud types prior to running the radiation scheme within the runtime of the simulations. Most classification schemes like that of Rogers (2010; further referred to as the "traditional" classification), which is an adaptation of Steiner et al.'s (1995) classification, depend on reflectivity and requires a comparison of neighboring grid cells to determine the precipitation type. But, to execute this classification algorithm within model runtime is computationally impractical. As the radiation scheme is run column-by-column, we desire a similar column-by-column approach for the classification algorithm. So, to determine the precipitation type of each grid cell, we developed an adapted version of Sui et al.'s (2007) classification, which determines the cloud mode based on the microphysics within the column. Although dependent on the microphysics scheme, Sui et al. (2007) found that their column-by-column approach produced reasonable results. The cloud partitioning method of Sui et al. (2007) is explained in further detail in the next subsection.

To build confidence in our algorithm, we compared our results to a traditional reflectivity-based classification from Rogers (2010) offline. As mentioned previously in Chapter 1, convective and stratiform precipitation have distinct and well-established vertical motion profiles. As part of our validity check, we produced these profiles for the new algorithm and compared them to that of the traditional reflectivity approach. Although we make this comparison to a reflectivity-based classification, we neither expect nor desire our results to perfectly match that of the classic reflectivity classification because the motivation behind each algorithm is different. The traditional algorithm is designed to determine the cloud mode based on low-level reflectivity and, essentially, rain rate. However, reflectivity is more sensitive to large rain drops and high rain rates, which are more common of convective regions. This could result in an underestimation or incorrect classification of stratiform and anvil regions, which have low rain rates or are non-raining. Since cloud–radiation interaction is not limited to strongly precipitating clouds, we have designed our algorithm with the goal of capturing this broader population of radiatively interactive clouds.

Most classification schemes have limited categories of precipitation. They often include categories for convective and stratiform and a third category that changes depending on the algorithm. The scheme by Rogers (2010) includes anvil as its third category and Sui et al.'s (2007) classification contains a mixed category that is between convective and stratiform. Different cloud types are expected to have different radiative forcing, which we seek to disentangle and understand. Therefore, we developed our algorithm to include the following categories: deep convective, shallow convective, congestus, stratiform, anvil, and non-raining. In summary, we seek to develop an approach that can be effectively applied "online" during numerical model runtime, captures the bulk convective and stratiform behavior as validated using well-established traditional classification approaches and paradigms of vertical motion, and includes additional classification sub-types on the basis that they likely have very distinct radiative forcing.

2.2.1 Description and Development

Sui et al.'s (2007) precipitation classification scheme is a column-by-column approach based on microphysical variables. They define a cloud ratio (CR) that compares the ice water path (IWP; the vertically integrated sum of ice, snow, and graupel mixing ratios) to the liquid water path (LWP; the vertically integrated sum of cloud and rainwater mixing ratios), calculated a CR = IWP/LWP, to distinguish between convective and stratiform regions (Sui and Li 2005). Assuming stratiform regions are dominated by ice and convective regions by liquid water, the CR can determine the cloud mode (Sui et al. 2007). We chose to use an adapted version of this classification using ad hoc thresholds, to add more precipitation categories, and to validate it against characteristic bulk vertical motion profiles for our model data set.

The classification process for our algorithm is summarized in **Figure 2.1**. The first step deems a grid cell non-raining if it falls below the total water path (TWP; the sum of IWP and LWP) threshold of 0.1 mm. We found a TWP threshold to be a necessary cutoff to exclude many grid columns identified as containing spurious (i.e., small magnitude) hydrometeor amounts associated with negligible rainfall and radiative forcing. This TWP cutoff compared to the traditional algorithm's TWP frequency is found in **Figure 2.2**, which demonstrates that most grid cells identified by the traditional classification as stratiform or convective have a TWP greater than our threshold. This comparison between our TWP threshold and the traditional classification indicates that by applying our specific TWP threshold, we are not greatly limiting the stratiform

and convective cells we can identify with our classification. Adjustments to the TWP threshold primarily effects shallow convective and anvil domain fractions (not shown).

Next, the convective and stratiform categories are separated by a CR threshold, as in Sui et al. (Sui et al. 2007). Columns with a CR < 2 are considered convective and columns with CR ≥ 2 are considered stratiform. This CR threshold as compared to the traditional classification cloud mode distributions is depicted in **Figure 2.3**, which demonstrates our CR threshold of 2 is positioned between the maximum frequency of convective and stratiform regions as identified by the reflectivity approach. This comparison indicates that our CR threshold will likely distinguish between convective and stratiform regions correctly based on the reflectivity-based classification. Convective regions are further divided between deep convective, congestus, and shallow convective by various column-integrated mixing ratios. Grid cells are marked shallow if they fall below a rain mixing ratio threshold of 0.1 mm. Deep convective is separated from congestus by a graupel mixing ratio threshold of 10^{-4} mm, with deep convective regions exceeding this threshold, on the basis that deep convective would have stronger updrafts and, therefore, a greater graupel mixing ratio. Stratiform is separated from anvil when columns exceed a rain mixing ratio of 0.01 mm, accounting for stratiform having more liquid water content than anvil. While we lack a means for assessing these thresholds in relation to the traditional algorithm, we can check how reasonable their vertical motion profiles are, which is detailed in the following subsection.

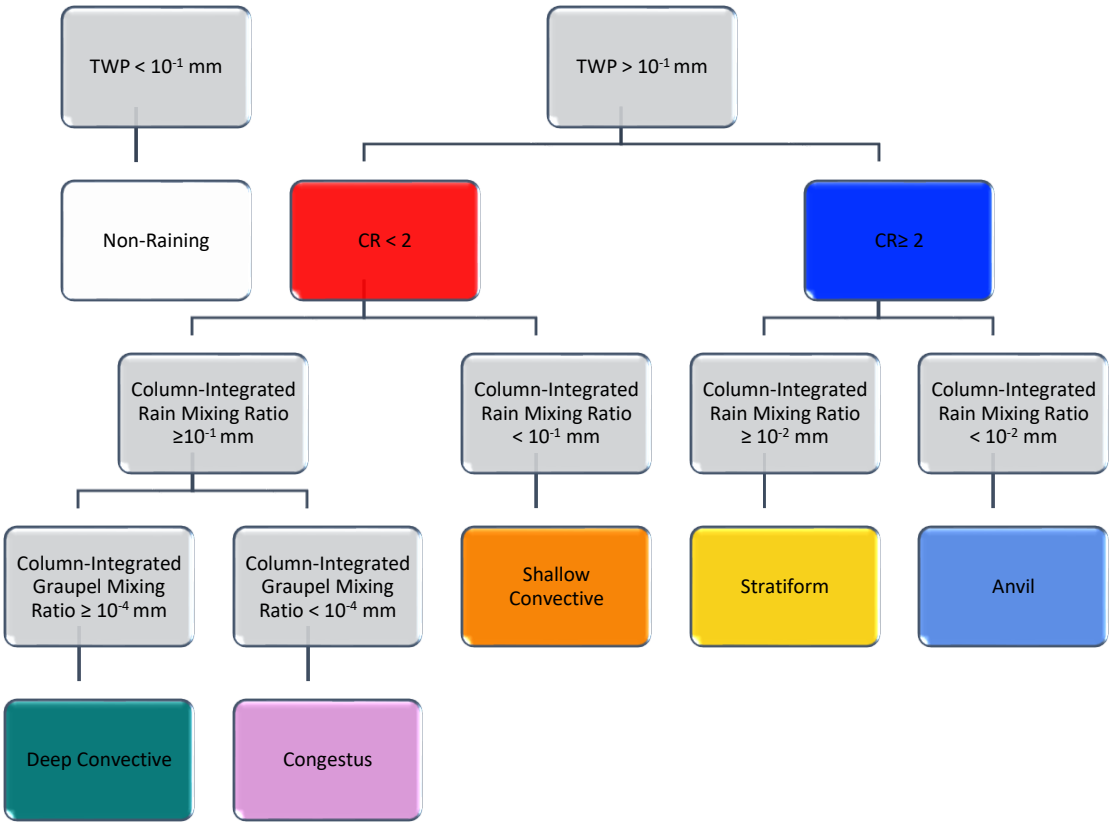

Figure 2.1: Flow chart summarizing the categorization process for our precipitation classification algorithm.

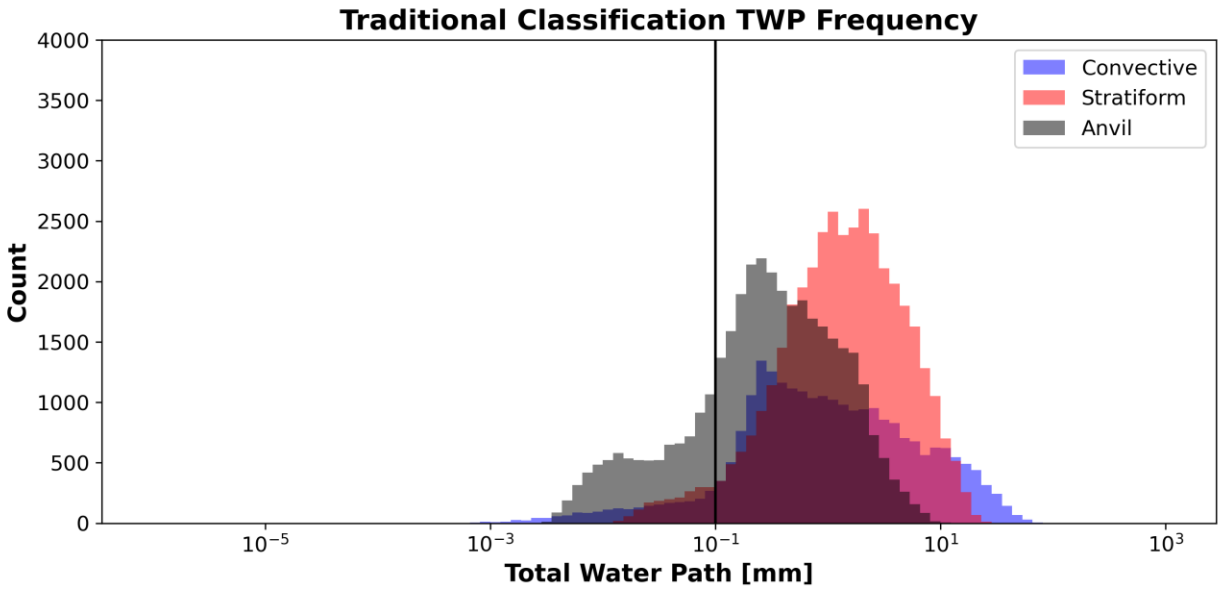

Figure 2.2: TWP frequency for the traditional classification. The convective mode is in blue, the stratiform mode is in red, and the anvil mode is in black. The vertical black line indicates the TWP threshold for our algorithm. Figure shows the first member of Haiyan CTL at the timestep 36 hours.

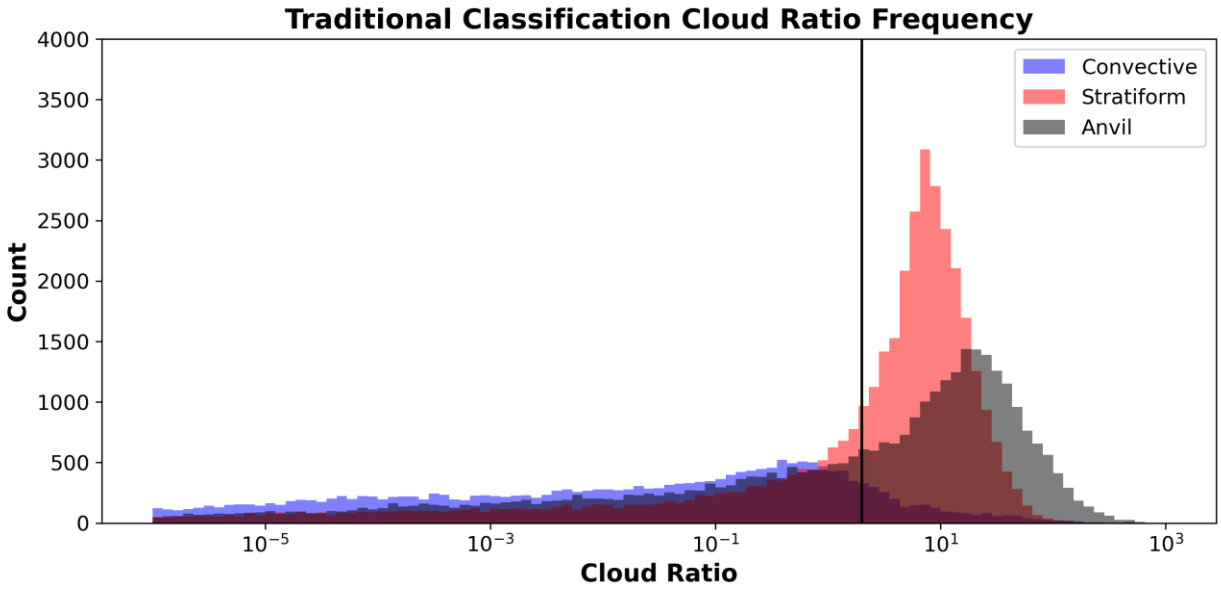

Figure 2.3: The CR frequency for the traditional classification. The convective mode is in blue, the stratiform mode is in red, and the anvil mode is in black. The vertical black line indicates the CR threshold for our algorithm. Figure shows the first member of Haiyan CTL at the timestep 36 hours.

2.2.2 Comparison and Validation

We perform the first check to determine the performance of our classification by looking at the domain percentage of each precipitation category. These values are listed in **Table 2.1** along with the traditional reflectivity classification. The new classification marks more grid cells within the domain as precipitating while also increasing the number of points identified as anvil and stratiform compared to the traditional algorithm. The increase in these percentages indicates that our algorithm is more sensitive to cloudy columns with lower rain rates, which is an expected and intended result, given our objectives. A visual display of the precipitation identification in **Figure 2.4** confirms the increase in identified cells with cloud and the greater number of points containing stratiform or anvil. The classification remains consistent across ensemble members, with the first 5 shown in **Figure 2.5**.

Table 2.1: Comparison of cloud type domain fraction between the new classification (deep convective, congestus, shallow convection, anvil) and the traditional classification (convective, stratiform, and anvil). Table contains values for the first member of Haiyan CTL at the timestep 36 hours.

Area Fraction by Cloud Type				
Cloud Type	New Classification		Traditional Classification	
	# of Points	Domain Fraction (%)	# of Points	Domain Fraction (%)
Deep Convective	12,629	1.42	N/A	N/A
Congestus	12,144	1.37	N/A	N/A
Shallow Convective	34,582	3.89	N/A	N/A
Convective Total	59,355	6.68	25,066	2.82
Stratiform	54,867	6.18	39,599	4.46
Anvil	53,112	5.98	36,569	4.12
Stratiform + Anvil	107,979	12.16	76,168	8.58
Precipitating Points	167,334	18.84	101,234	11.4
Non-Precipitating Points	720,666	81.16	786,766	88.6

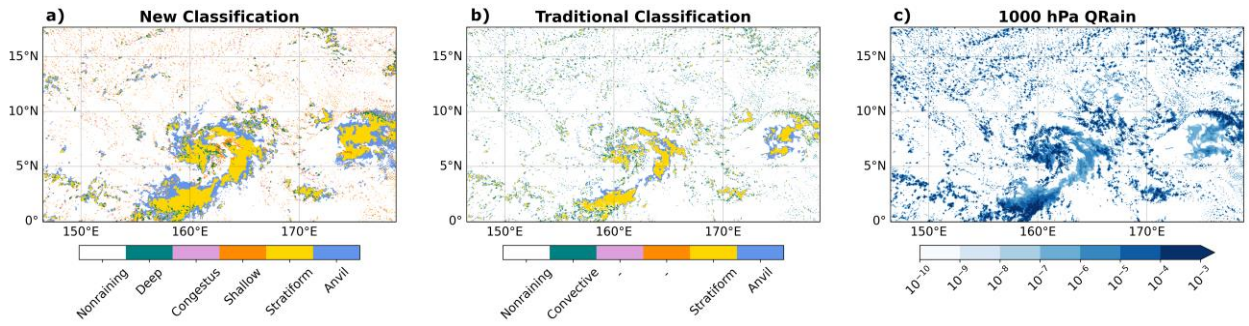

Figure 2.4: Maps comparing a) our new classification scheme, the b) traditional reflectivity classification, and c) 1000 hPa rain mixing ratio. Colors indicate non-raining (white), deep convective (a; teal), convective (b; teal), congestus (a; pink), shallow convective (a; orange), stratiform (yellow), and anvil (blue). All panels show the first member of Haiyan CTL at the timestep 36 hours.

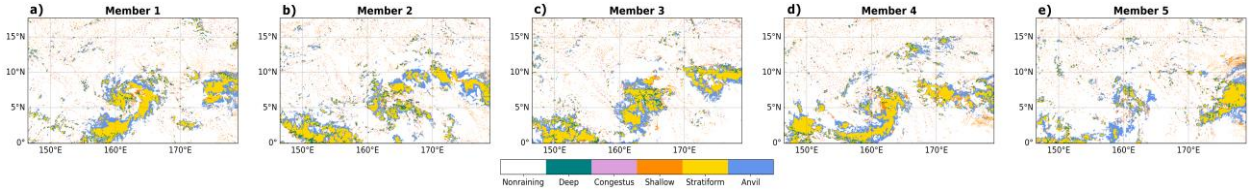

Figure 2.5: Maps depicting cloud classification for the first five members using the new microphysics-based classification. All panels show Haiyan CTL at 36 hours.

The placement of cloud types can also provide insight to the performance of the classification algorithms. In a convective cluster, we would expect to see deep convective surrounded by stratiform, and with anvil on the edges. In the traditional classification, convective regions are often located on the edges or in small clusters without stratiform surrounding it. However, in our classification, more of the stratiform and anvil cloud regions enveloping the deep convection are identified (**Figure 2.4 – a**). Additionally, the small clusters of cells marked as convective in the traditional algorithm to the north of the precursor disturbance are further identified as shallow convective in our algorithm.

As a means for validating our classification, we show the vertical motion (w) profiles averaged for each cloud type in the new classification alongside the traditional scheme in **Figure 2.6**. Because convective and stratiform profiles have distinct and well-established vertical motion profiles (Steiner et al. 1995; Houze 2004), comparing these profiles assures the merits of the classification. We expect to see deep convective regions to have a bottom-heavy profile, with a maximum in the mid-levels. The deep convective region from the new classification does produce

a w-profile that maximizes around 550 hPa (**Figure 2.6 – a**). Both the congestus and the shallow convective regions also have bottom-heavy profiles with peaks around 850 hPa and 900 hPa, respectively. The average of the model grid columns of all three convective types results in a profile consistent with the shape of traditional convective classification profile, albeit with a smaller magnitude. This consistency can be expected because the convective profile from the traditional algorithm includes all three convective types. The new algorithm's stratiform profile yields the expected top-heavy profile with upward motion in upper levels and downward motion in the lower levels (**Figure 2.6 – b**). The anvil profile is like that of the stratiform profile but with a smaller magnitude. In comparison with the traditional approach, the profiles are similar in shape but with slight differences in magnitudes and with the new classification having a 100 hPa higher inflection point. Overall, we conclude from these comparisons that the new classification produces the expected vertical motion profiles.

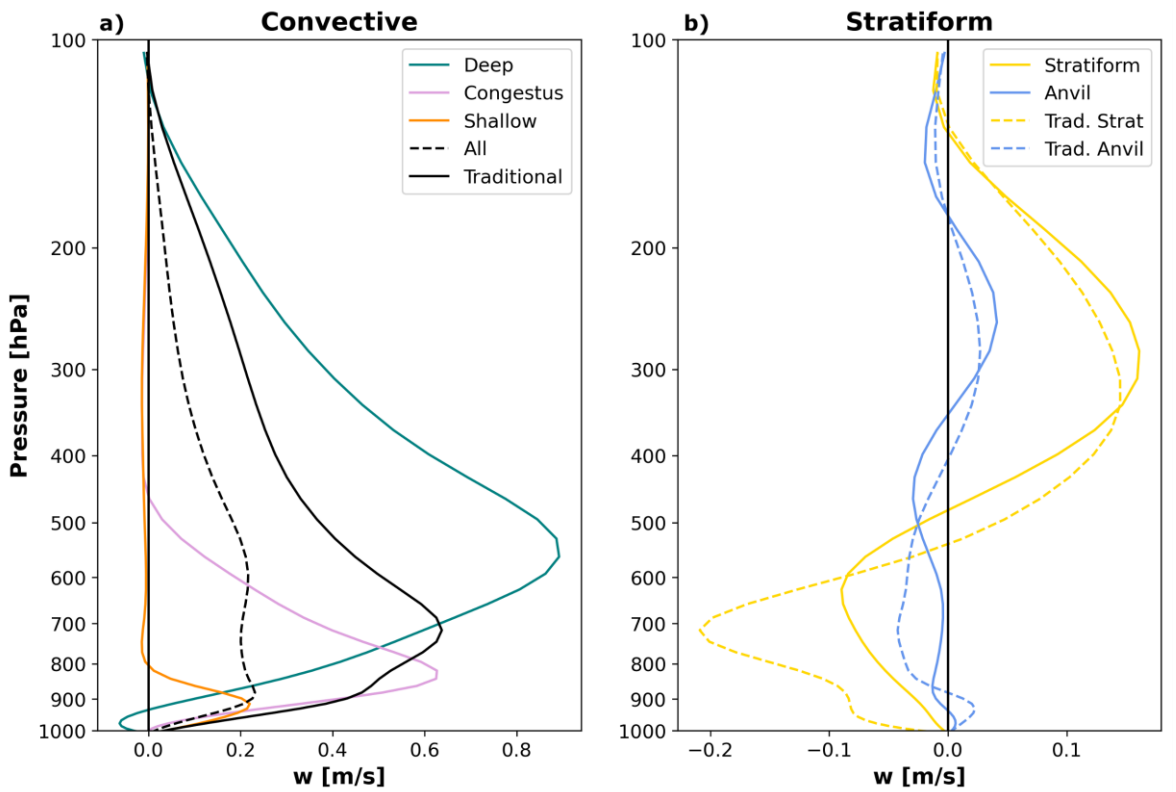

Figure 2.6: Vertical motion (w) profiles of a) convective and b) stratiform regions. The microphysics classification is broken into deep convective (a; teal), congestus (a; pink), shallow convective (a; orange), stratiform (b; solid yellow), and anvil (b; solid blue). The profile of all convective types from the microphysics classification is in dashed black. The traditional classification w-profiles are categorized into convective (a; solid black), stratiform (b; dashed yellow), and anvil (b; dashed blue). Both panels show the first member of Haiyan CTL at the timestep 36 hours.

Based on the assessments above, we conclude that the new classification algorithm accurately identifies precipitation types for this model output. The scheme is more feasible to run in a numerical model than traditional reflectivity-based schemes as it is based on microphysics thresholds and is a column-by-column approach. This allows for precipitation classification within the framework of models without the need of neighboring cell information, which is computationally cumbersome in highly parallelized frameworks commonly used for convective-scale modeling. However, this approach does have some weaknesses. By having the precipitation classification based on microphysics thresholds, the scheme inherently relies on specific hydrometeor behavior and treatment. Different microphysics schemes have vastly different treatments of hydrometeors (Morrison et al. 2020) and would hence inevitably require modification to apply to other microphysics schemes. Despite the likely sensitivity to the

microphysics scheme and the required adjustment of thresholds, the algorithm is deemed suitable to meet our science objectives, as introduced in Chapter 1.

3 Longwave Radiative Feedback as a Function of Cloud Mode

This chapter will summarize and discuss the results addressing **SO 1**, i.e., determining the relative contribution of different cloud regions to the LW ACRE and the LW MSE variance term. Section 3.1 covers precipitation classification with respect to LW ACRE, while Section 3.2 addresses precipitation classification with respect to LW MSE variance. For both variables, we calculate the domain average for each cloud class as $\frac{Var\ Total_{cloud_class}}{Total\ Domain\ Points}$ and the class average is calculated as $\frac{Var\ Total_{cloud_class}}{Total\ Class\ Points}$. Both averages are calculated across all levels (1000 hPa – 50 hPa).

3.1 Atmospheric Cloud Radiative Effect (ACRE) and Cloud Radiative Forcing (CRF)

It is likely that different precipitation types provide different radiative forcing. As ACRE and CRF represent the direct forcing due to LW radiation, we seek to quantify each precipitation mode's contribution to these variables. Using our column-by-column based classification algorithm, we calculated the domain-averaged, and class-averaged LW ACRE. We exclude the first 12 timesteps as it is considered as "spin-up" time for the simulation. We also exclude the domain edges, 80 grid points on each side, from all calculations in the rest of this chapter. Stratiform and anvil modes contribute the most to the domain-averaged LW ACRE with averages around 10 W m^{-2} (**Figure 3.1**). Of the convective types, deep convective has the greatest contribution to the LW ACRE (~2.5 W m^{-2}), with congestus and shallow convective points providing the least radiative forcing to the domain average. The large contribution to the domain average by stratiform and anvil modes is partly due to the large area coverage of these regions, for example as depicted at 36 hours in **Figure 3.2**.

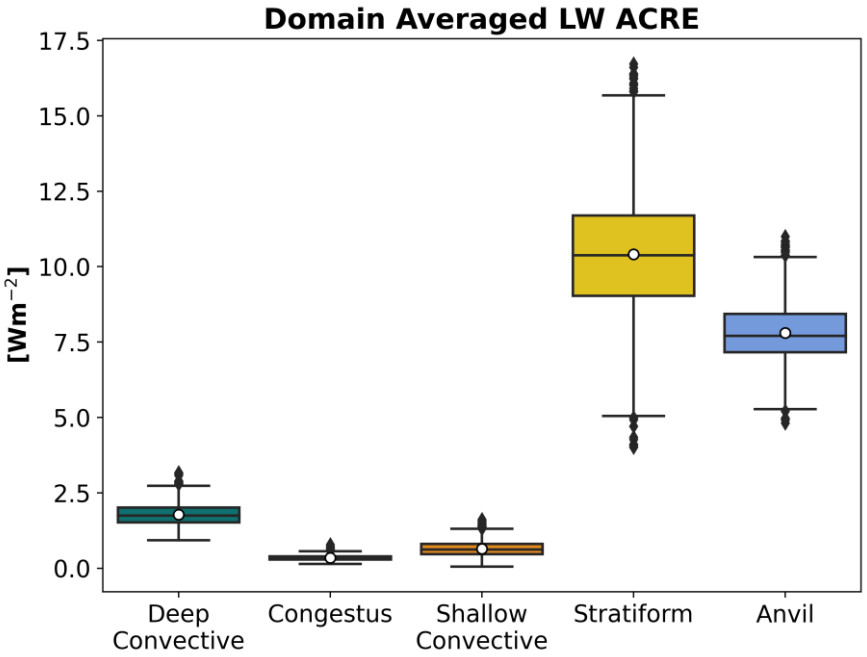

Figure 3.1: Boxplots of domain averaged LW ACRE by precipitation type. White circles indicate the mean value. Black diamonds represent outliers. Plots include values from all 10 members and 85 timesteps for Haiyan CTL.

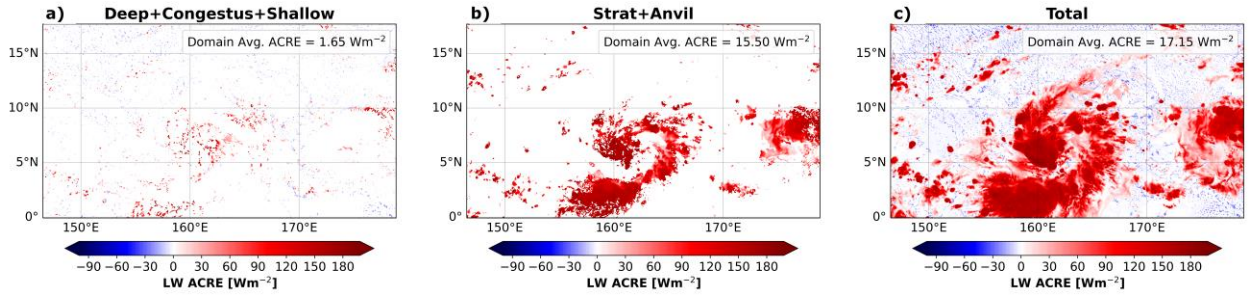

Figure 3.2: Maps showing the ACRE for a) convective categories, b) stratiform and anvil, and c) all categories. The legend contains the domain-averaged ACRE for the respective precipitation categories. All panels show the first member of Haiyan CTL at 36 hours.

But area coverage is not the only reason stratiform and anvil regions have the greatest domain-averaged LW ACRE. When we divide LW ACRE by only the number of grid cells identified within a specific cloud class, or the class average, stratiform and anvil regions also have the highest class averaged LW ACRE (**Figure 3.3**). They are almost an order of magnitude greater than that of the congestus and shallow convective types. Deep convective has the greatest LW ACRE value of the three convective modes, with an average value of ~85 W m^{-2}. This value is comparable in magnitude to that of stratiform and anvil regions, suggesting comparable radiative

forcing by these categories within a given column. Combining the class average LW ACRE with the area coverage of the stratiform and anvil modes explains their much larger contribution to the domain-averaged LW ACRE.

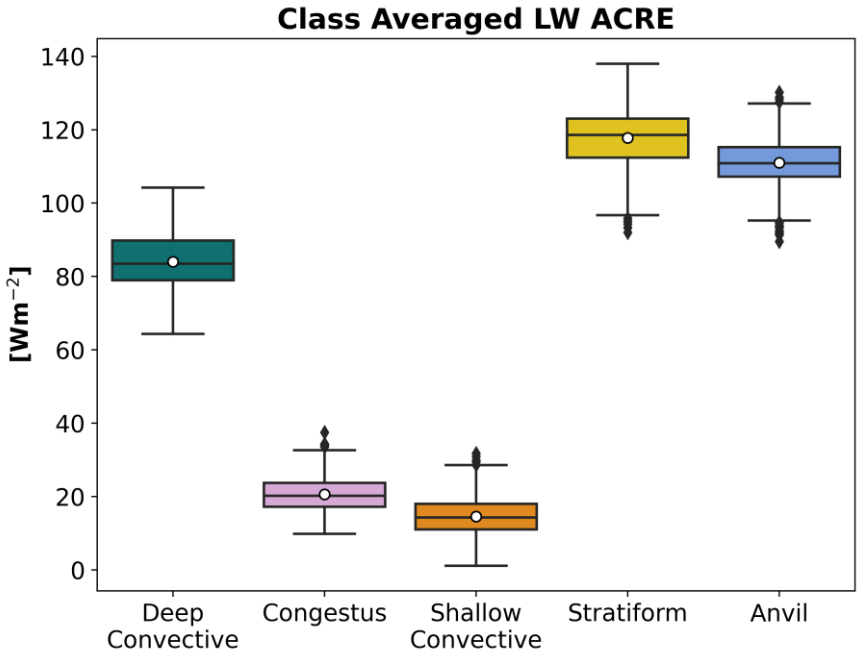

Figure 3.3: As in **Figure 3.1** but for class-averaged LW ACRE.

CRF profiles can provide insight to each precipitating type's ACRE class average value. Cloud modes with larger ACRE values have a deep layer of positive CRF (**Figure 3.4**). Stratiform and anvil modes are very comparable in CRF shape and magnitude. They have the largest positive layer from 200 hPa to the surface and with maxima around 5 K day^{-1} at 300 hPa, with strong cloud-top cooling above 200 hPa. Of the convective categories, deep convective has the deepest layer of positive CRF of 2 K day^{-1} from 200 hPa to the surface, with a small layer near 0 K day^{-1} between 400 and 500 hPa. Like stratiform and anvil, deep convective has a strong signature of cloud-top cooling above ~200 hPa. Congestus and shallow convective modes have maxima in the lower troposphere with cooling above, likely due to their low cloud-top height. Above 800 hPa, their CRF hovers around 0 Kday^{-1}. Departures from the zero line in the upper troposphere are likely a result of the algorithm's ability to only identify one cloud type for each column and may include values from high stratiform or anvil. These results are consistent with expectations of cloud depth based on mean vertical motion (**Figure 2.6**).

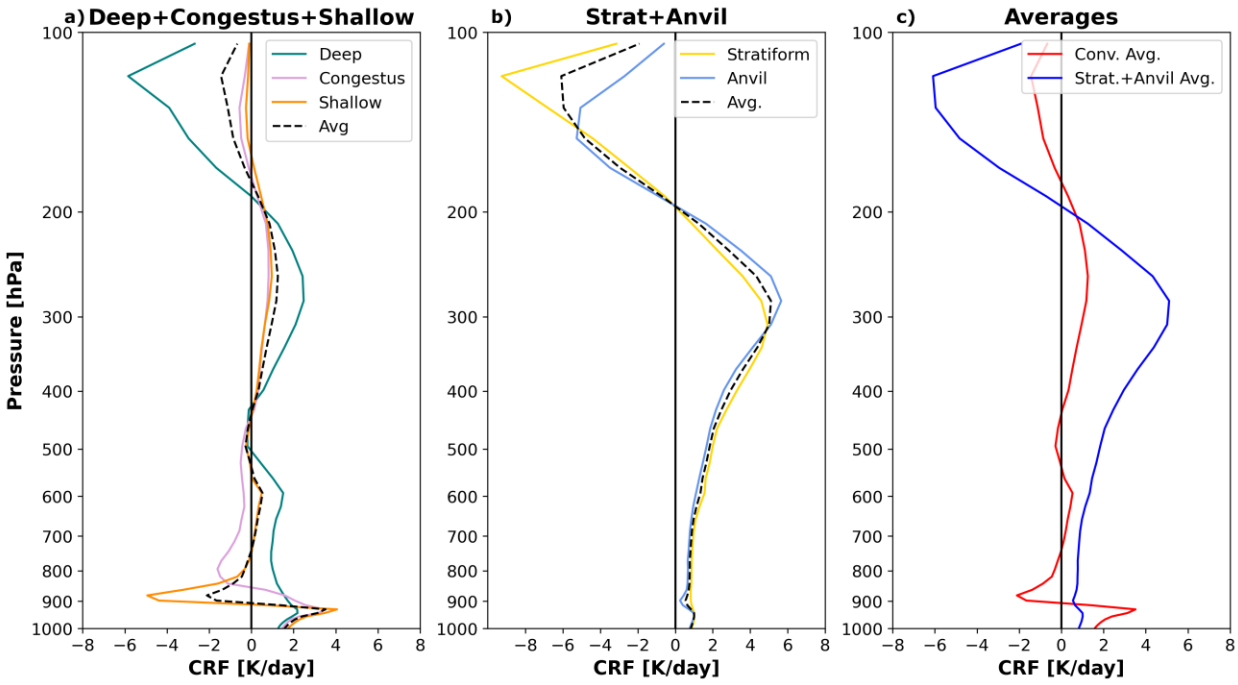

Figure 3.4: CRF vertical profiles of a) convective and b) stratiform/anvil regions. The microphysics classification is broken into deep convective (a; teal), congestus (a; pink), shallow convective (a; orange), stratiform (b; yellow), and anvil (b; blue). The averaged convective and stratiform/anvil profiles are in dashed black in a) and b). The convective (red) and stratiform/anvil (blue) are repeated in the third panel (c) for comparison.

3.2 Moist Static Energy Variance

The MSE budget is a tool that allows us to assess and quantify upscale development and intensification of convection. This tool has been used to assess the influence of radiative feedback in relation to both self-aggregation (Wing and Emanuel 2014) and TC genesis (Ruppert et al. 2020). Our interest in this budget is primarily in the LW-source term as it has been shown to be the dominating term for initiating and maintaining convective organization in self-aggregation (Wing and Emanuel 2014; Wing and Cronin 2016). The LW MSE variance term ($\widehat{h}'NETLW'$) is the correlation between the anomaly of density-weighted vertical integral of frozen MSE ($\widehat{h}'$) and the anomalous column LW radiative flux convergence ($NETLW'$). A detailed explanation for the calculation of this variable can be found in Wing and Emanuel (2014).

For our diagnosis, we calculate MSE as

$$MSE = DSE + L_v q = c_p T + gz + L_v q, \qquad \text{Equation 3.1}$$

where DSE is the dry static energy, L_v is the latent heat of vaporization, q is the water vapor mixing ratio, c_p is the specific heat, T is the temperature, g is the gravitational acceleration, and z is the height. Including the frozen term of MSE is expected to have a negligible qualitative impact on our results. Next, to diagnose the LW MSE variance term, we subtract the horizontal average from both vertically integrated MSE and the net LW radiation. We then calculate the covariance between MSE and the net LW radiation before dividing by the MSE variance. The domain average calculation of this MSE variance corresponds to the source term in the MSE variance budget (Wing and Emanuel 2014).

By masking by cloud type, we can understand the individual roles of each precipitation mode. Once again, stratiform and anvil regions contribute the most to the domain average LW MSE variance term with stratiform dominating with an average of about 0.035 day^{-1} (**Figure 3.5**). The stratiform regions also have the highest LW MSE variance of all the cloud types when averaged by class (**Figure 3.6**). Congestus and shallow convective points have the lowest class averaged LW MSE variance, as may be anticipated from LW ACRE (**Figure 3.3**). Surprisingly, deep convective regions have the second highest LW MSE variance, almost matching that of stratiform. Anvil's class average follows convective with a value of 0.25 day^{-1} compared to stratiform and deep connective's averages of about 0.4 day^{-1}. Like the LW ACRE, the stratiform and anvil regions have greater areal coverage as compared to the convective regions (**Figure 3.7**). Even though deep convective regions had one of the highest class-averaged LW MSE variance term, its small areal coverage does not allow the cloud type to contribute considerably to the domain average unlike stratiform and anvil regions.

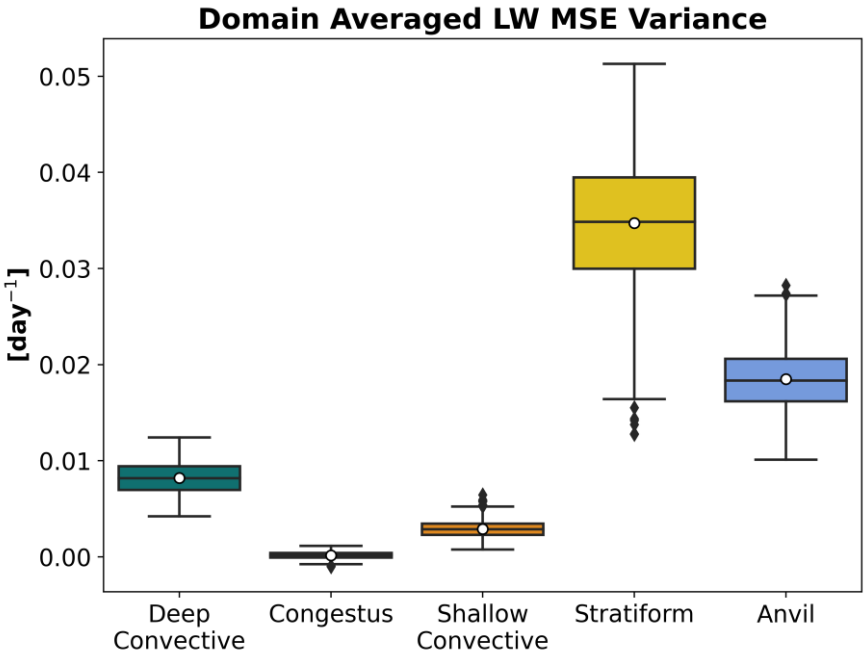

Figure 3.5: As in **Figure 3.1** but for LW MSE variance.

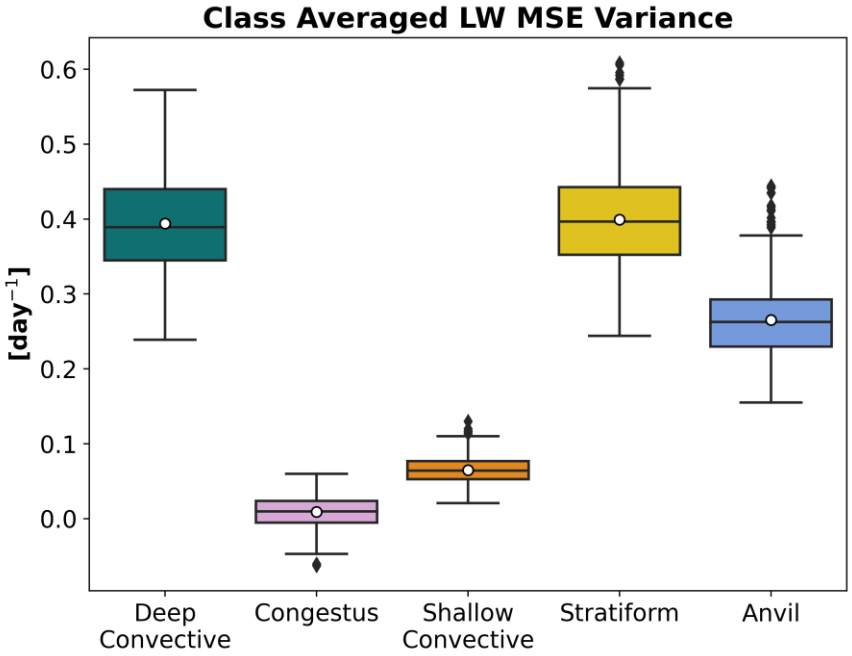

Figure 3.6: As in **Figure 3.3** but for LW MSE variance.

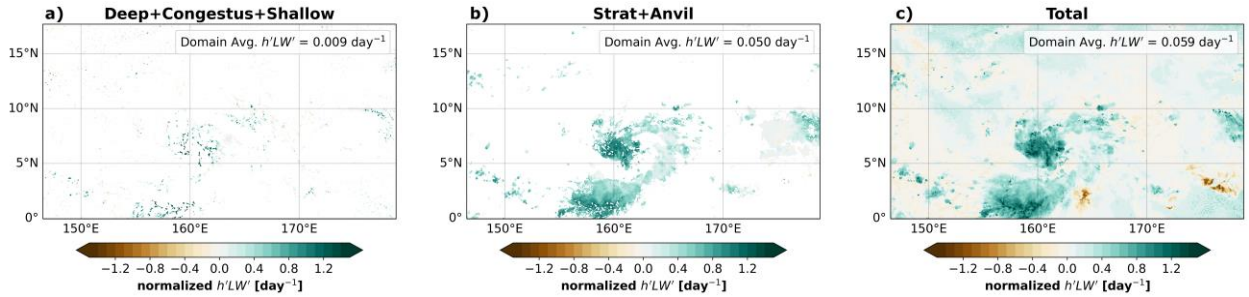

Figure 3.7: As in **Figure 3.2** but for LW MSE variance source term.

The high LW MSE variance of stratiform and anvil combined with their expansive areal coverage hints at their unique importance for supporting upscale convective development in the tropics by amplifying MSE variance. Although deep convective regions also have high values of LW MSE variance, the small regional coverage of this cloud type likely limits its impact on convection from an MSE perspective. There are certainly other ways in which deep convective regions encourage upscale development. But these findings emphasize the influence stratiform and anvil regions may also have on convection initiation and maintenance specifically through radiative forcing, which have not been previously considered.

4 The Stratiform Radiation Effect in a TC Context

This chapter will summarize and discuss results concerning **SO 2**, which focuses on the role different cloud types' CRF has in TC genesis and development, and **SO 3**, which looks into the dynamical mechanisms why CRF in specific cloud types, especially that of stratiform, promote and accelerate TC genesis. Because we are concentrating on TC genesis, we will only use data from the first 9 ensemble members, as Member 10 did not form a tropical cyclone and produced a nonsensical storm track in the CTL due to the midlevel vortex remaining very weak throughout the simulation (**Figure 4.1**). To diagnose the TC tracks, we use an object-based tracking procedure following (Davis et al. 2006) and Rios-Berrios et al. (2018). The first step is to smooth the 600-hPa absolute vorticity field. Then, we standardize and mask the 600-hPa absolute vorticity field anywhere it is less than three standard deviations, locate its all-simulation-time maximum, and track that forward and backward through all time steps. We constrain our analysis in this chapter to a 300-km radius surrounding this tracked 600-hPa midlevel vortex. This radius narrows our focus from the whole domain to where storm development occurs, while still being broad enough to consider the pre-genesis storm environment. We also use the TC tracks of CTL for the analysis of all sensitivity tests. In this way, we can compare the same region of the domain between tests. As our analysis focuses on the hours immediately following the start of the sensitivity tests, the midlevel vortex in the sensitivity tests should be in a similar location to that of CTL.

As a reminder, our sensitivity tests include turning off CRF in all cloud regions (NCRF), in convective regions (C-NCRF), in stratiform and anvil regions (SA-NCRF), and stratiform regions only (S-NCRF). To determine cloud type and switch CRF off/on in each type within these sensitivity tests, we use our new cloud classification discussed in Chapter 2. Although we do not repeat the radiative forcing diagnoses for each of these sensitivity tests, the results presented in Chapter 3 directly indicate the forcing that is retained and modified in these sensitivity tests.

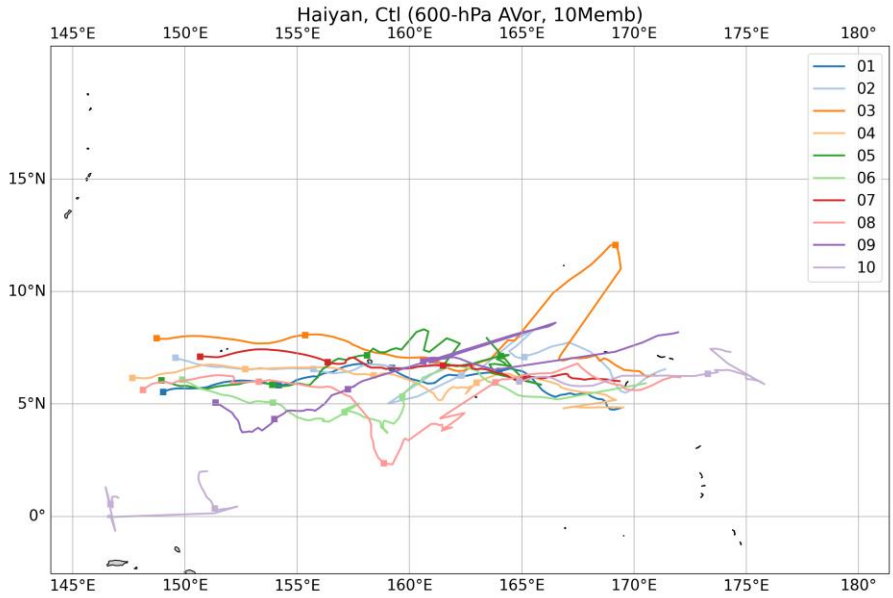

Figure 4.1: Tracks for all 10 ensemble members following a 600-hPa absolute vorticity maximum in the CTL Haiyan simulation. Member 10 is in light purple.

4.1 Development of Haiyan

4.1.1 Evolution of Cloud Fraction

With the ability to diagnose 5 different cloud types, we wish to understand how these cloud types evolve with time in the developing TC storm region. In the CTL simulation, stratiform has the most variability and experiences the most change throughout the simulation but has the greatest percentage of areal coverage within the analyzed radius (**Figure 4.2**). Congestus has the smallest percentage and remains relatively unchanged throughout. Coverage by anvil and shallow convective regions stays consistent as well with some slight variations. Deep convective has a noticeable increase in its cloud fraction between 24 and 48 hours before experiencing a dip in coverage and subsequently increasing again. Both stratiform and deep convective increase in areal fraction within 48 hours of TC genesis, which begins around hour 78 (**Figure 4.3**). Here we define genesis as a sustained increase in the maximum wind like that of rapid intensification (RI), or an increase 15 m/s increase in the maximum wind over 24 hours (Kaplan and DeMaria 2003). In the last 18 hours of the CTL simulation, the 850 hPa maximum wind increases about 10 m/s. Although this change falls slightly short of the RI threshold, the trend of the maximum wind by the end of CTL is to continue to increase, suggesting the start of an RI event and TC genesis. The simulations described by Ruppert et al. (2020) are integrated further into the future and support

this point, though they do not include the sensitivity tests we describe here. The increase in stratiform cloud fraction prior to the likely RI of our simulated Haiyan agrees with observational studies showing an expansion of stratiform regions prior to an RI event (Tao et al. 2017).

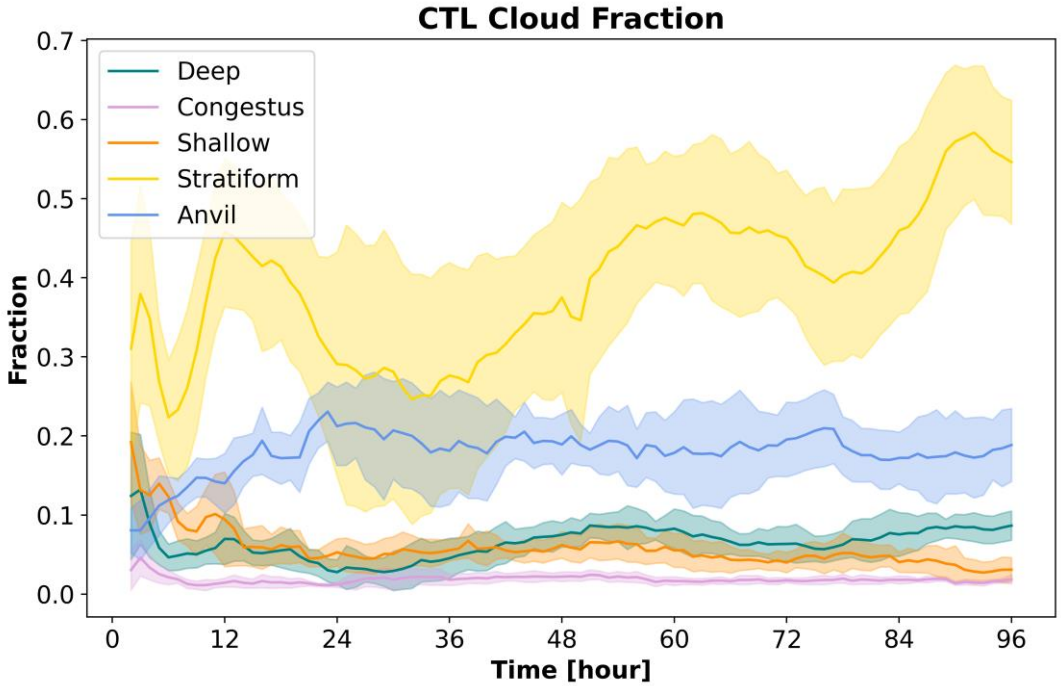

Figure 4.2: Cloud fraction for 9 members of CTL Haiyan. The solid line indicates the hourly average across members. Shading indicates 95% confidence intervals. Categories include deep convective (teal), congestus (pink), shallow convective (orange), stratiform (gold), and anvil (blue). Area fractions are calculated within a 600 km radius around the domain 600 hPa vorticity maximum.

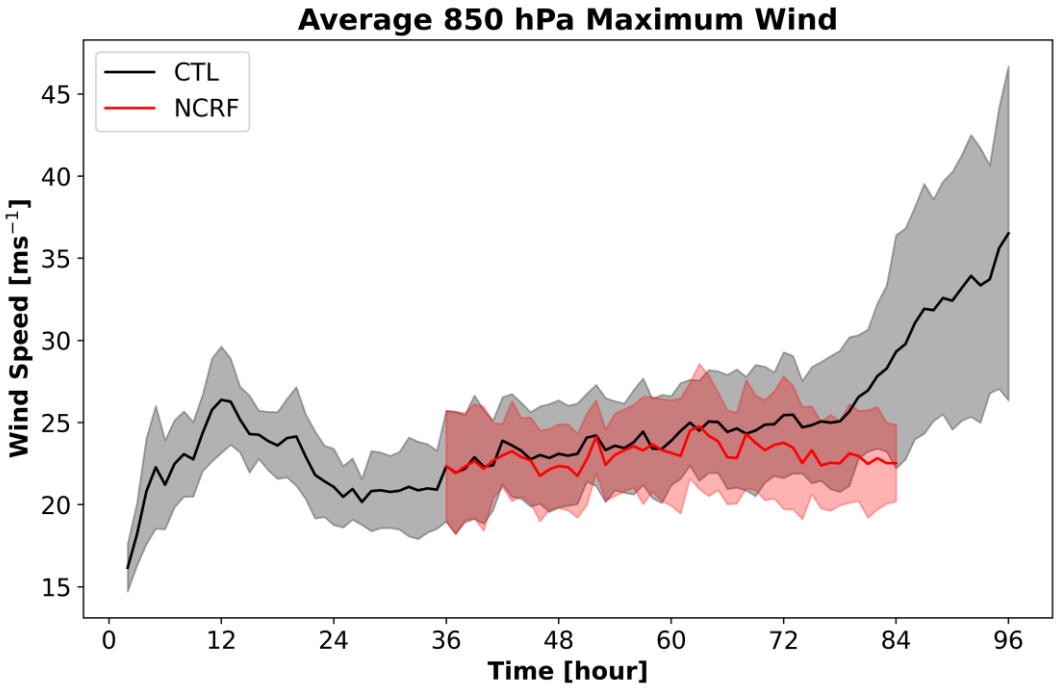

Figure 4.3: Timeseries of a 9-member average of the maximum 850 hPa wind within a 600 km radius of the 600 hPa midlevel vortex for Haiyan. Lines indicate the mean for CTL (black) and NCRF (red) tests. Shading represents the 95% confidence interval.

In the sensitivity tests, the development of the cloud types matches that of CTL for most cloud modes with congestus and shallow convective being the most similar (**Figure 4.4**). There are slight differences between the anvil cloud fractions in CTL and the sensitivity tests, but no clear pattern emerges. There are greater changes in the deep convective and stratiform modes, with a similar arrangement in the order of the sensitivity tests. In both categories, CTL has the greatest mean cloud fraction and NCRF has the lowest. SA-NCRF follows the NCRF test closely while C-NCRF is the most similar of the sensitivity tests to CTL. The convective and stratiform categories may have the sensitivity tests arranged in a similar order, but the magnitude of the differences between the tests are greater in stratiform. This difference is likely due to stratiform having the greatest cloud fraction of all the cloud modes, and therefore the greatest radiative forcing as suggested by the MSE feedback term (**Figure 3.6**). Comparing these results to the maximum wind show that only the C-NCRF test has an uptick in its maximum wind by the end of the simulation (**Figure 4.5**). Although the change is on too short of a timescale to conclude whether an RI event was occurring by the end of C-NCRF, the closer alignment of its max wind and stratiform cloud coverage to CTL suggests it may be entering RI and TC genesis, the only sensitivity test to do so.

C-NCRF's greater stratiform cloud fraction and greater LW CRF is likely the driving factor of C-NCRF's rise in maximum wind speed.

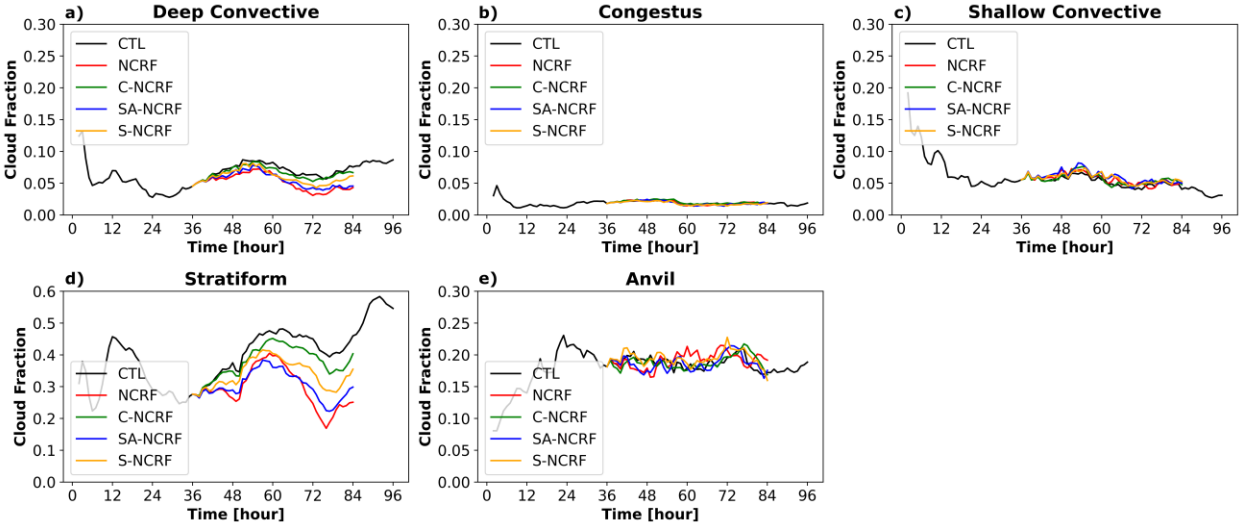

Figure 4.4: Cloud fraction hourly means for 9 members for Haiyan tests CTL (black), NCRF (red), C-NCRF (green), SA-NCRF (blue), and S-NCRF (yellow). Cloud types include a) deep convective, b) congestus, c) shallow convective, d) stratiform, and e) anvil. Area fractions are calculated within a 600 km radius around the domain 600 hPa vorticity maximum.

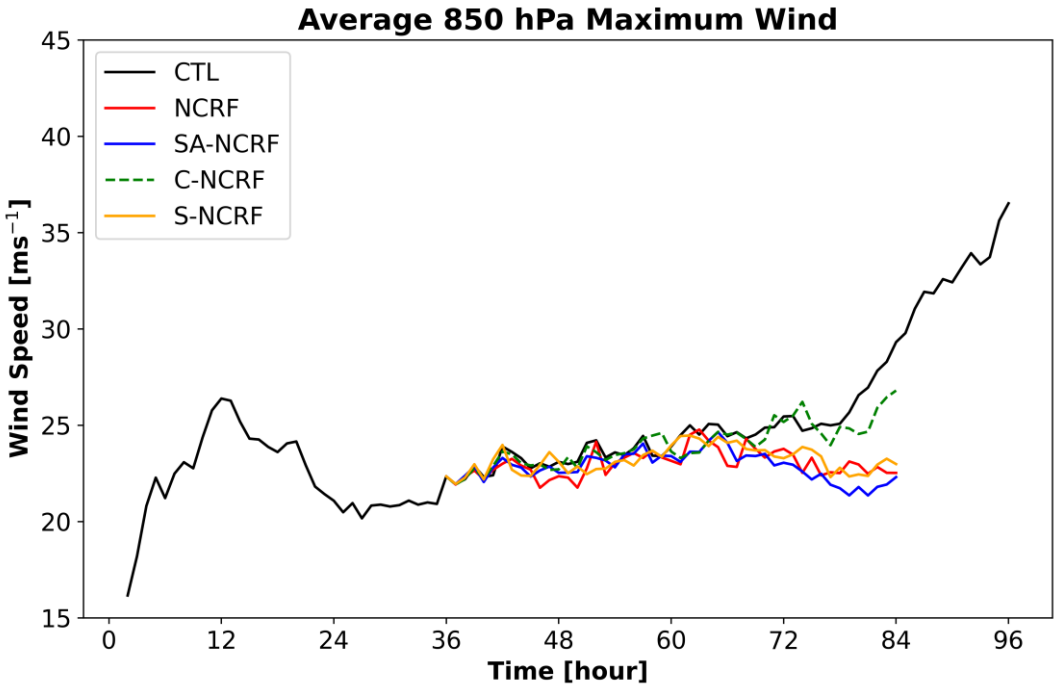

Figure 4.5: Time series of a 9-member average of the maximum 850 hPa wind within a 600 km radius of the 600 hPa midlevel vortex for Haiyan. Lines indicate the mean for CTL (black), NCRF (red), SA-NCRF (blue), C-NCRF (dashed green), and S-NCRF (yellow).

4.1.2 Midlevel Vortex Intensification

We seek to understand how CRF impacts TC development. **Figure 4.6** compares the strength of 600 hPa absolute vorticity, a proxy for TC precursor strength, between the CTL and NCRF simulations. The midlevel vortex is a TC precursor, so it can, therefore, provide a perspective on the development of TC genesis (Dunkerton et al. 2009; Wang 2012; Gjorgjievska and Raymond 2014). Without the addition of CRF, the mean values of 600 hPa absolute vorticity begin to depart within 12 hours of restart from CTL. Although the confidence intervals always overlap between CTL and NCRF, their growing difference with time is apparent. With a longer NCRF test, we expect the difference in their 600 hPa absolute vorticity to become strongly significant. NCRF's weaker vorticity illustrates the impact CRF makes on TC intensification and aligns with previous studies such as Yang et al. (2021), which highlight CRF's ability to accelerate the development of the midlevel vortex.

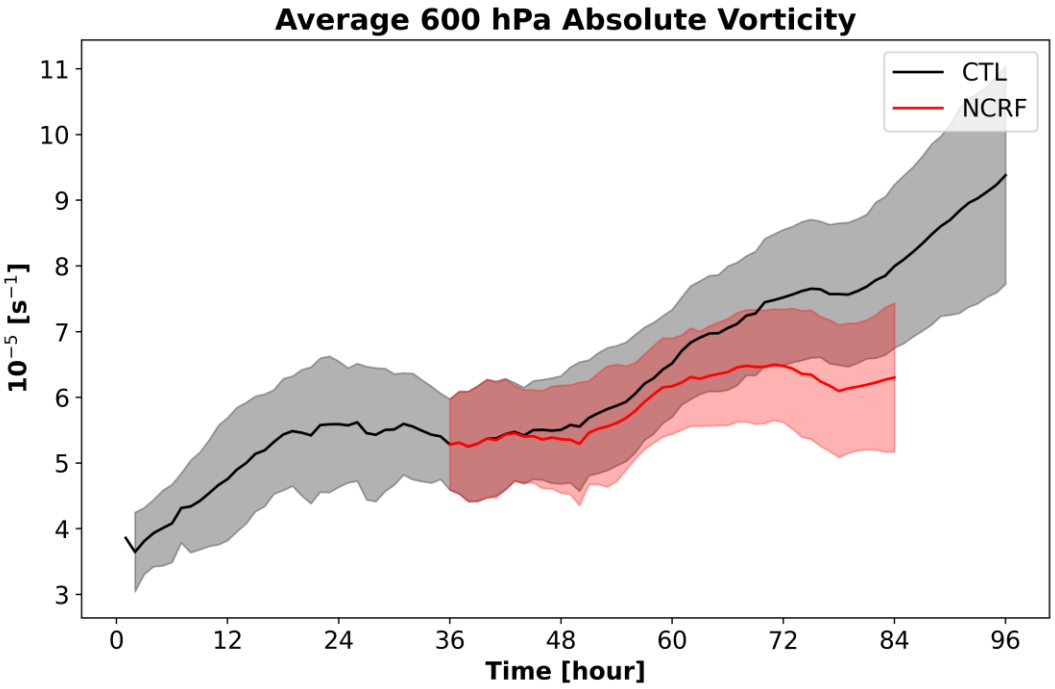

Figure 4.6: As in **Figure 4.3** but for 600 hPa absolute vorticity.

However, the focus of this thesis is not only on the importance of CRF on TC development, but the role that CRF in different cloud classes, specifically stratiform, has on TC genesis and intensification. Comparing CTL to the sensitivity tests shows the relative importance of cloud type CRF on TC development (**Figure 4.7**). C-NCRF has the greatest vorticity development of the sensitivity tests (i.e., is most similar to CTL), followed by S-NCRF. NCRF has the weakest vorticity with SA-NCRF being the third weakest. As NCRF does not include any LW CRF, it is no surprise that it has the weakest vorticity.

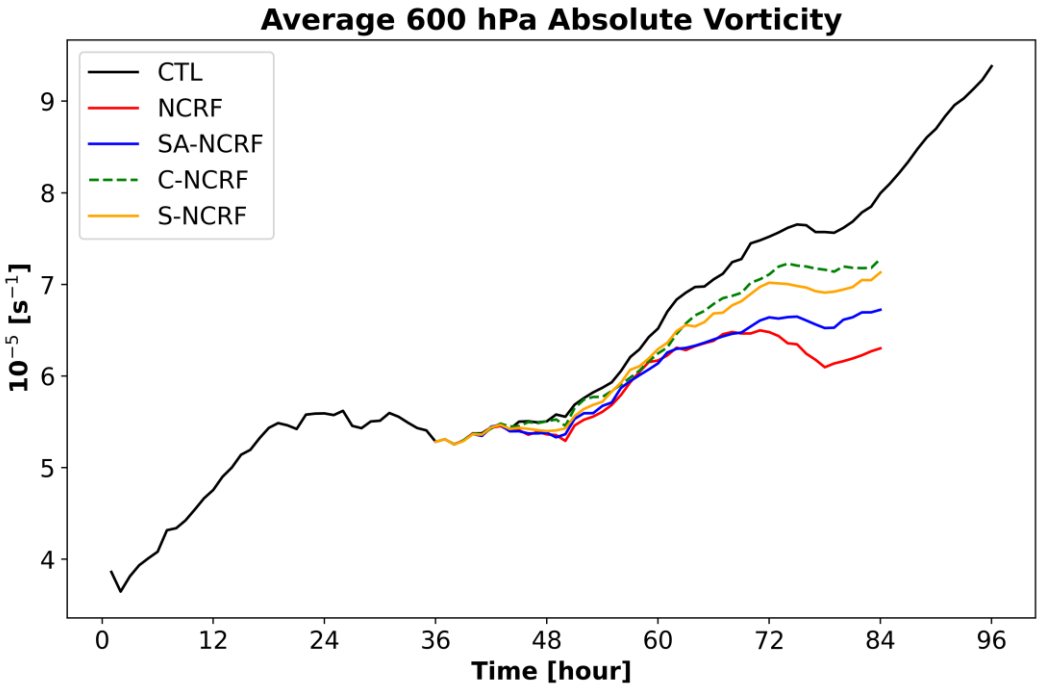

Figure 4.7: As in **Figure 4.5** but for 600 hPa absolute vorticity.

In Chapter 2, we found that stratiform and anvil regions had the highest LW ACRE values both in terms of the domain and class averages (**Figure 3.1**; **Figure 3.3**). These regions also had high LW MSE variance contributions (**Figure 3.5**; **Figure 3.6**). Turning CRF off in these regions results in a midlevel vortex of a similar strength to that in the NCRF test. Convective type regions contributed the least to the domain averaged ACRE and LW MSE variance term, despite deep convective having large class averages in both variables. When CRF is only retained in convective regions, it is like not having CRF at all, as the areal coverage of convective regions is extremely small compared to that of stratiform and anvil. Reversing the roles of stratiform and anvil with convective regions in the C-NCRF test shows the impact of removing CRF is minimized when CRF remains in stratiform and anvil areas. Removing the role of stratiform CRF only in the S-NCRF test had a slightly greater impact on the midlevel vortex's strength than removing convective CRF. This could indicate the key role of anvil regions in developing and organizing deep convection. This finding is surprising because of stratiform's dominance in the LW ACRE and LW MSE variance term.

4.2 Impacts of Stratiform CRF on Dynamical Mechanisms Promoting TC Genesis

The previous section concentrated on the impact of turning CRF on and off in different cloud regions and how it affected TC genesis and development. We found that stratiform and anvil region CRF contributed the most to the genesis of Haiyan within our simulation, which is consistent with the findings of Chapter 3. The aim of this section is to investigate through what dynamical and thermodynamical mechanisms CRF in different cloud regions works to promote and accelerate TC genesis.

4.2.1 Stratiform CRF Weakens Downward Vertical Mass Flux (VMF)

In Chapter 1, we hypothesized that it was CRF, particularly in stratiform regions, that weakened the drying caused by stratiform downdrafts. To test this, we use vertical mass flux (VMF; ρw), or density times vertical motion, to diagnose downdraft frequency and behavior. When we turned CRF off from the formation of Haiyan, the NCRF test formed more frequent and stronger downward motion in stratiform regions as opposed to CTL as early as one hour after the start of the sensitivity tests (**Figure 4.8 - a**). This signal increases in magnitude as time increases, for example, at hour 6 (**Figure 4.9**). The increase in frequency and strength of downdrafts in mid- to low levels in NCRF is indicative of CRF's ability to weaken stratiform downdrafts. Additionally, excluding CRF leads to stronger and more frequent weak updrafts above 300 hPa (**Figure 4.9 - a**). The result of these two effects on VMF is greater mean rising motion in the lower to mid-troposphere and sinking motion in the upper troposphere in CTL relative to NCRF. Although we only show these CFADs for stratiform regions, the results are extremely similar if we include all precipitating areas (not shown). While stratiform downdrafts are argued to be between the surface and mid-levels (i.e., the melting layer around 550 hPa) (Steiner et al. 1995; Houze 2004), the impacts shown in **Figure 4.9** indicate changes in downdrafts over a much deeper layer. We hypothesize that this is due to the nature and depth of thermal forcing by CRF, which will be discussed in the next section.

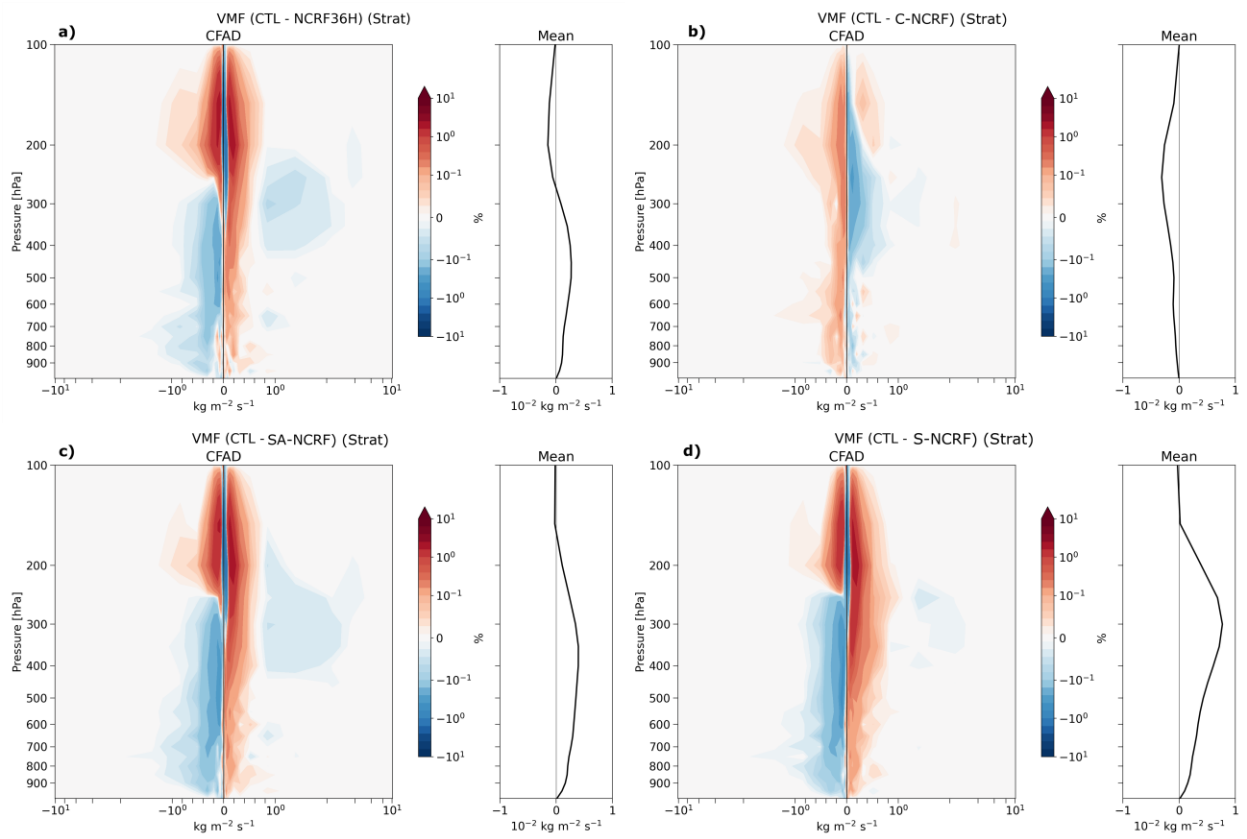

Figure 4.8: Contoured frequency by altitude diagrams (CFADs) of the difference in vertical mass flux (VMF) between CTL and a) NCRF ; b) C-NCRF ; c) SA-NCRF ; and d) S-NCRF one hour after the start of the sensitivity tests. Red shading indicates CTL has a greater frequency and blue shading indicates the sensitivity test has a greater frequency. Mean profiles to the left show the mean difference between the tests.

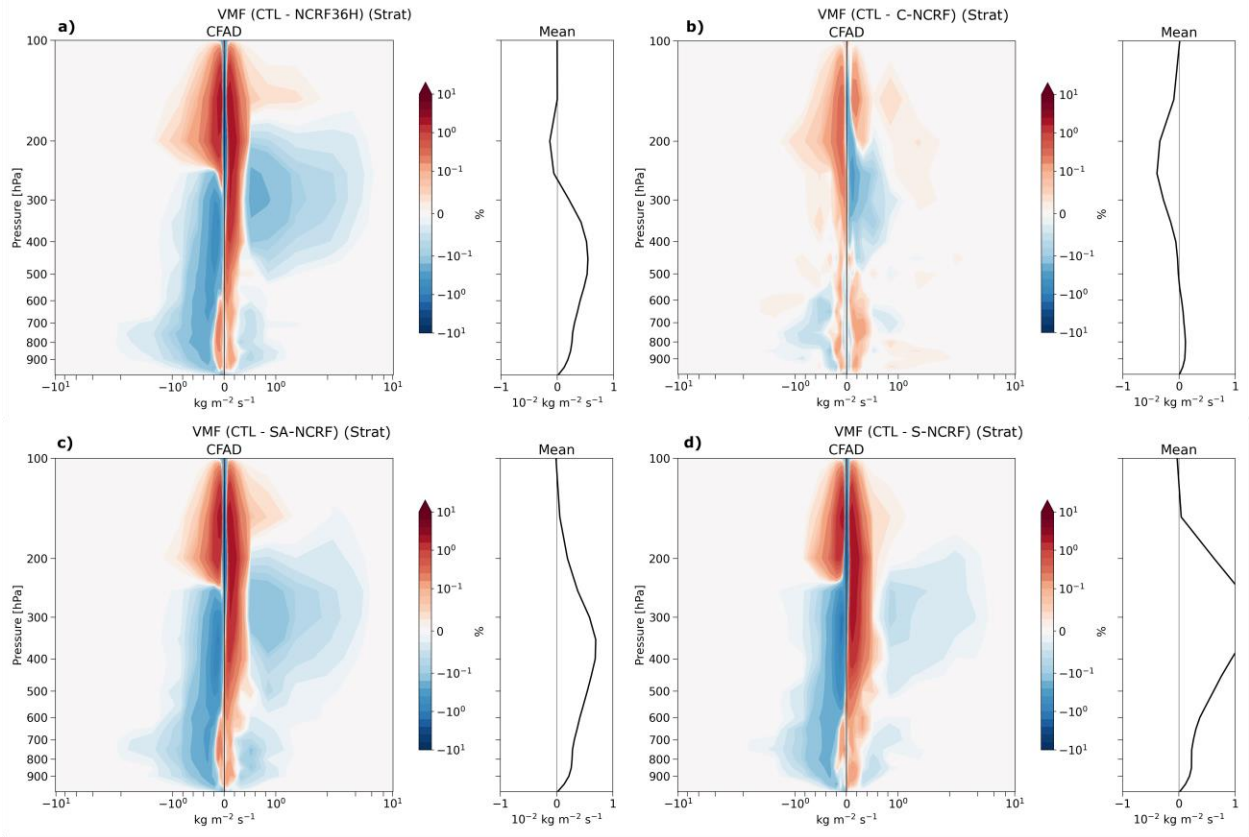

Figure 4.9: Same as **Figure 4.8** but for 6 hours after the start of the sensitivity tests.

Further isolating CRF in different cloud regions allows us to identify how CRF in different cloud types contributes to the weakening of stratiform downdrafts. When convective CRF is removed, there is little impact on stratiform VMF in the mid- to low levels except for a slight increase in downdraft frequency as compared to CTL (**Figure 4.9 – b**). The difference between CTL and C-NCRF maximizes at 250 hPa with CTL having an average weaker VMF by about $0.5x10^{-2}$ kg m^{-2} s^{-1}. This difference seems to account for the more frequent and stronger updrafts that the NCRF test experienced as compared to CTL. Therefore, convective CRF may assist in increasing downward vertical motion in the upper levels.

The opposite test in which convective CRF is turned on and stratiform and anvil CRF is turned off in SA-NCRF reveals many nearly identical signatures to those noted in the NCRF test (**Figure 4.9 – c**). Although the SA-NCRF test contains grid points with both downdrafts and updrafts of a greater magnitude than CTL, the mean profile shows that CTL has greater mean upward VMF of about $0.5x10^{-2}$ kg m^{-2} s^{-1}. Further separating stratiform CRF from anvil in the S-NCRF test unveils that neglecting stratiform CRF maximized the difference in VMF between CTL

and S-NCRF by more than 10^{-2} kg m^{-2} s^{-1} at 300 hPa (**Figure 4.9 – d**). This difference accounts for more than the average difference between CTL and NCRF. Together, these results suggest that the exclusion of convective CRF explains the signature of increased downward motion in the upper troposphere in the NCRF and C-NCRF tests relative to CTL. Stratiform CRF's ability to decrease downdraft frequency and magnitude in the upper levels is likely diminished by that of convective CRF. The results found in Chapter 3 support these findings by emphasizing the role stratiform and anvil regions play in increasing the ACRE of the domain.

The sensitivity tests reveal that stratiform CRF has an important role in weakening and decreasing the frequency of stratiform downdrafts in our simulation of Haiyan, while convective CRF tends to increase their magnitude and frequency in the upper levels. The differences in frequency between the CTL and the sensitivity tests do appear small and have an order of magnitude around 10^{-3} kg m^{-2} s^{-1}. However, considering that we are evaluating stratiform downdrafts, which by definition have weak vertical motion, on hourly timescales, we expect the differences to be small. The previous section also noted that excluding CRF had an impact on the development of the midlevel vortex. So, these differences, while small, are expected to play an important role in explaining these impacts on the midlevel vortex.

4.2.2 Stratiform CRF and an Increase in Positive Buoyancy

In the previous subsection, we found that CRF, especially in stratiform regions, weakens downward VMF. Virtual potential temperature can be used as an indicator of buoyancy as an interpretation of these changes since buoyancy strongly influences vertical motion. We calculate the virtual potential temperature anomaly (θ_v') by subtracting the 300 km radius mean from an outer 600 km radius average. With CRF switched off, the mean θ_v' is colder below 900 hPa and in the upper mid-levels between 500 and 200 hPa (**Figure 4.10 – a**). This denser air in the boundary layer and upper mid-levels of the simulations without CRF helps explain the increased frequency and strength of the downward vertical motion previously discussed. With CRF turned off in convective regions only, there is little difference in θ_v' compared to when CRF is left on for all cloud regions (**Figure 4.10 – b**). The minimal change in θ_v' without convective CRF supports the notion that stratiform and anvil CRF have the most influence of all the cloud types in controlling buoyancy and, thus, downward vertical motion. Between stratiform and anvil CRF, it is more difficult to determine their separate influence on buoyancy especially in the low levels. In the

upper mid-levels, stratiform CRF appears to account for most of the increased warming and resulting upward movement (**Figure 4.10 – d**).

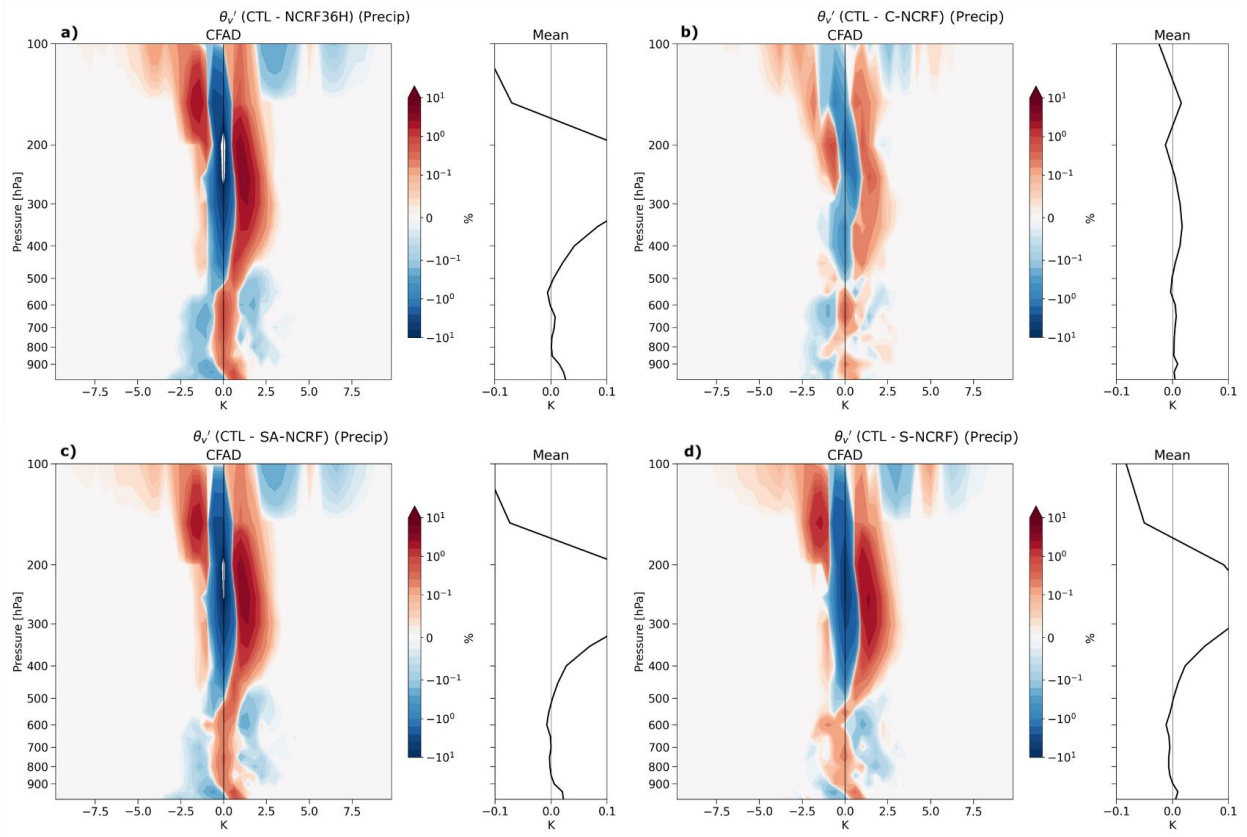

Figure 4.10: Same as **Figure 4.9** but for anomalous virtual potential temperature θ_v'.

4.2.3 Stratiform CRF and a Moister Storm Column

The second part of our hypothesis is that that decreasing stratiform downdrafts promotes TC genesis by moistening the storm column and increasing MSE. Because MSE can increase due to an increase in DSE (**Equation 3.1**), we show latent energy ($L_v q'$), the latent heat of vaporization multiplied by the water vapor mixing ratio anomaly, to highlight the change in MSE due to changes in moisture. The latent energy anomaly is calculated like that of θ_v' in the previous subsection. Following our hypothesis, we expect CTL to have a higher $L_v q'$ in the mid to low levels due to weakened downdrafts and more buoyancy. We assess this as the deviation from the background mean because the sensitivity tests do not have significant changes in this background (not shown). With CRF switched off, CTL does have higher $L_v q'$ from 200 hPa to the surface (**Figure 4.11 – a**).

The NCRF test has a higher frequency around the zero line except below 700 hPa where the NCRF test has more points with a weaker $L_v q'$. This difference indicates CRF's ability to increase MSE and moisture through $L_v q'$.

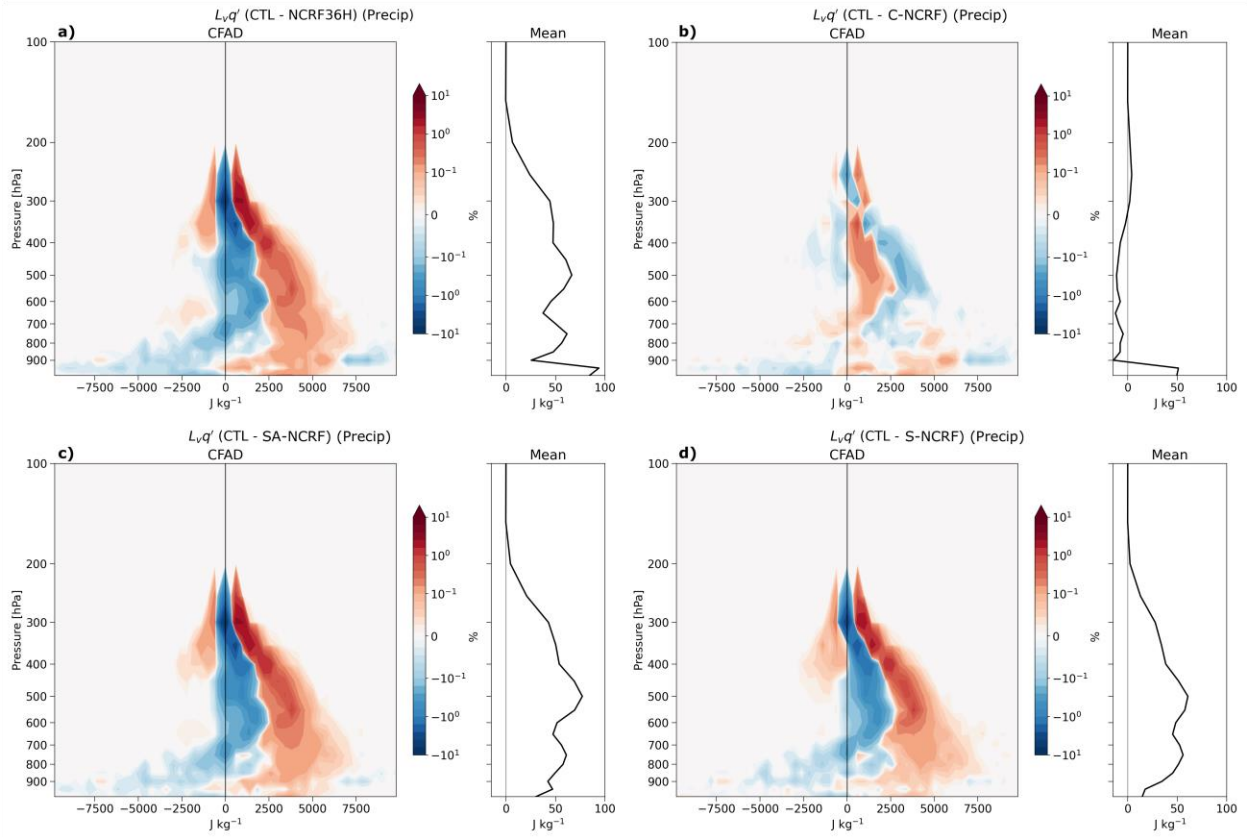

Figure 4.11: Same as **Figure 4.9** but for $L_v q'$.

Through the sensitivity tests, we can evaluate the impact of cloud type on $L_v q'$. When convective CRF is turned off, the mean difference between CTL and C-NCRF is less than 25 J kg^{-1} (**Figure 4.11 – b**). In this case, CTL has weaker $L_v q'$ in the mid-levels with a positive difference greater than 50 J kg^{-1} below 900 hPa. This implies that the inclusion of convective CRF results in drying effects while highlighting stratiform and anvil CRF's role in increasing $L_v q'$. This point is further supported by the SA-NCRF difference with CTL as the mean difference profile and difference CFAD look like that of CTL and NCRF (**Figure 4.11 – c**). S-NCRF differentiates the role between anvil and stratiform CRF in increasing $L_v q'$. With stratiform CRF off, most of the change in $L_v q'$ between CTL and NCRF is due to the absence of stratiform CRF as the S-NCRF

test looks similar in shape and magnitude to that of the NCRF and SA-NCRF tests (**Figure 4.11 – d**). The results found in Chapter 3 support these findings by emphasizing the role stratiform and anvil regions play in upscale convective development based on their ability to increase the LW MSE source term within the domain.

5 Summary and Conclusions

The overarching goal of this thesis was to identify the relative roles of different cloud types on tropical convective organization through their radiative forcing. As the first step to accomplish this goal, we developed a novel cloud classification algorithm. This new algorithm classifies cloud types based on the microphysical variables available from numerical model output on a column-by-column basis. The algorithm can classify a total of 5 cloud types including deep convective, congestus, shallow convective, stratiform, and anvil. Based on a comparison between our classification and a traditional reflectivity-based algorithm, our classification produces reasonable vertical motion profiles for the bulk convective and stratiform regions and detects a much greater sample of cloudy columns in the model domain, which is important for our research objectives.

This new algorithm holds a few advantages as compared to the traditional reflectivity approach. Our classification does not require neighboring grid cell information as it is run column-by-column, thus making it computationally efficient for running within the framework of a numerical model. The classification is also dependent on full-column microphysical sampling as opposed to low-level reflectivity, allowing for more grid cells with low rain rates to be identified as containing cloud. This algorithm therefore enables us to capture cloud–radiative forcing more comprehensively. Finally, our cloud classification identifies 5 cloud types, including separating convective regions into three unique classes, unlike other classifications that typically only have three total cloud classes. However, a disadvantage to this algorithm is its likely sensitivity to different microphysics schemes based on its threshold approach. Despite this disadvantage, this novel approach to cloud classification allows for more questions to be answered on the influence of cloud type, including the three science objectives of this thesis related to cloud–radiation feedback.

The first objective of this thesis was to determine the LW ACRE and LW MSE variance term for different cloud types. We ran a WRF simulation of Super Typhoon Haiyan (2013) focused on the pre- and genesis period to evaluate the LW ACRE and LW MSE variance of different cloud types. We hypothesized that stratiform regions would support convective organization the most through LW ACRE and MSE variance term. For the LW ACRE, we found that stratiform and anvil contributed the most to the domain averaged ACRE and had greater class-averaged ACRE ($\frac{Var\ Total_{cloud_class}}{Total\ Class\ Points}$) than that of the other types, indicating their important

contribution to the direct LW radiative forcing. For the LW MSE variance term, stratiform and anvil again contributed the most to the domain average. However, the class averages revealed that deep convective was on par with stratiform regions, resulting in those two classes having the highest class-averages. Anvil was third highest, followed by shallow and congestus, which were much weaker. While the class-averaged LW MSE variance indicates that the localized forcing by deep convective, stratiform, and anvil clouds is comparable, anvil and stratiform clouds dominate in supporting convective upscale development owing to their much greater area coverage.

Our second objective was to identify the relative importance of different cloud type CRF on the promotion and acceleration of TC genesis, hypothesizing that stratiform would have the most impactful role. In addition to the CTL simulation, we ran sensitivity tests as restarts from the CTL that excluded CRF in varying cloud regions. From these simulations, we found that excluding convective CRF alone made the least impact on TC genesis and produced a storm most similar to the CTL. Excluding CRF in stratiform and anvil regions resulted in a TC genesis timeline that differed most greatly from that of the CTL. The stratiform and anvil region CRF therefore likely promoted the genesis of Haiyan.

Besides understanding what cloud type CRF contributed the most to TC genesis acceleration, we also wanted to understand through what dynamical mechanisms CRF worked to accomplish this task, which constituted our third objective. We hypothesized that stratiform CRF decreases stratiform downdraft strength and frequency and thereby moistening the storm column. We found that stratiform and anvil CRF reduced downdrafts in stratiform regions, with stratiform CRF accounting for most of the reduction. The decreased frequency and magnitude of stratiform downdrafts is related to the warmer storm column, especially below 900 hPa, by stratiform and anvil CRF. Stratiform and anvil CRF also helped moisten the storm column by bringing in a greater value of the moisture component of MSE, specifically $L_v q'$. As TC genesis requires enhanced moisture in the mid-levels, stratiform and anvil CRF contribute the most to increased moisture as compared to other cloud regions through the influence of vertical motion and downdrafts.

Future work will include running a similar analysis on Hurricane Maria (2017) as well as longer simulation runtimes for the sensitivity tests. Longer simulations would allow for more conclusive results on the stratiform CRF's ability to promote TC genesis. In addition, we wish to

run sensitivity tests for Haiyan and Maria with restarts at a different time of day to see the effects of the diurnal cycle on CRF in TC genesis.

6 Reference List

Ahmed, F., and C. Schumacher, 2015: Convective and stratiform components of the precipitation-moisture relationship. *Geophys Res Lett*, **42**, 10,453-10,462, https://doi.org/10.1002/2015GL066957.

Bell, M. M., and M. T. Montgomery, 2019: Mesoscale processes during the genesis of Hurricane Karl (2010). *J Atmos Sci*, **76**, 2235–2255, https://doi.org/10.1175/JAS-D-18-0161.1.

Bister, M., and K. A. Emanuel, 1997: The genesis of Hurricane Guillermo: TEXMEX analyses and a modeling study. *Mon Weather Rev*, **125**.

Bony, S., and Coauthors, 2015: Clouds, circulation and climate sensitivity. *Nat Geosci*, **8**, 261–268, https://doi.org/10.1038/NGEO2398.

Bretherton, C. S., M. E. Peters, and L. E. Back, 2004: Relationships between water vapor path and precipitation over the tropical oceans. *J Clim*, **17**, 1517–1528, https://doi.org/10.1175/1520-0442(2004)017.

——, P. N. Blossey, and M. Khairoutdinov, 2005: An energy-balance analysis of deep convective self-aggregation above uniform SST. *J Atmos Sci*, **62**, 4273–4292, https://doi.org/10.1175/JAS3614.1.

Davis, C. A., B. Brown, and R. Bullock, 2006: Object-based verification of precipitation forecasts. Part I: Methodology and application to mesoscale rain areas. *Mon Weather Rev*, **134**, 1772–1784, https://doi.org/10.1175/MWR3145.1.

Dunkerton, T. J., M. T. Montgomery, and Z. Wang, 2009: Tropical cyclogenesis in a tropical wave critical layer: Easterly waves. *Atmos Chem Phys*, **9**, 5587–5646, https://doi.org/10.5194/ACP-9-5587-2009.

Gjorgjievska, S., and D. J. Raymond, 2014: Interaction between dynamics and thermodynamics during tropical cyclogenesis. *Atmos Chem Phys*, **14**, 3065–3082, https://doi.org/10.5194/ACP-14-3065-2014.

Gray, W. M., 1998: The formation of tropical cyclones. *Meteorology and Atmospheric Physics*, **67**, 37–69, https://doi.org/10.1007/BF01277501/METRICS.

Hendricks, E. A., M. T. Montgomery, and C. A. Davis, 2004: The role of "Vortical" Hot Towers in the formation of Tropical Cyclone Diana (1984). *J Atmos Sci*, **61**, 1209–1232, https://doi.org/10.1175/1520-0469(2004)061<1209:TROVHT>2.0.CO;2.

Houze, R. A., 2004: Mesoscale convective systems. *Reviews of Geophysics*, **42**, 1–43, https://doi.org/10.1029/2004RG000150.

Iacono, M. J., J. S. Delamere, E. J. Mlawer, M. W. Shephard, S. A. Clough, and W. D. Collins, 2008: Radiative forcing by long-lived greenhouse gases: Calculations with the AER radiative transfer models. *Journal of Geophysical Research: Atmospheres*, **113**, 13103, https://doi.org/10.1029/2008JD009944.

Kaplan, J., and M. DeMaria, 2003: Large-scale characteristics of rapidly intensifying tropical cyclones in the North Atlantic Basin. *Weather Forecast*, **18**, 1093–1108.

Manabe, S., and R. F. Strickler, 1964: Thermal equilibrium of the atmosphere with a convective adjustment. *J Atmos Sci*, **21**, 361–385, https://doi.org/10.1175/1520-0469(1964)021<0361:TEOTAW>2.0.CO;2.

Montgomery, M. T., and R. K. Smith, 2017: Recent developments in the fluid dynamics of tropical cyclones. *https://doi.org/10.1146/annurev-fluid-010816-060022*, **49**, 541–574, https://doi.org/10.1146/ANNUREV-FLUID-010816-060022.

Morrison, H., and Coauthors, 2020: Confronting the challenge of modeling cloud and precipitation microphysics. *J Adv Model Earth Syst*, **12**, e2019MS001689, https://doi.org/10.1029/2019MS001689.

Muller, C., and S. Bony, 2015: What favors convective aggregation and why? *Geophys Res Lett*, **42**, 5626–5634, https://doi.org/10.1002/2015GL064260.

Muller, C. J., and I. M. Held, 2012: Detailed investigation of the self-aggregation of convection in cloud-resolving simulations. *J Atmos Sci*, **69**, 2551–2565, https://doi.org/10.1175/JAS-D-11-0257.1.

Najarian, H., and N. Sakaeda, 2023: The influence of cloud types on cloud-radiative forcing during DYNAMO/AMIE. *Journal of Geophysical Research: Atmospheres*, **128**, e2022JD038006, https://doi.org/10.1029/2022JD038006.

National Centers for Environmental Prediction/National Weather Service/NOAA/U.S. Department of Commerce, 2015: NCEP GFS 0.25 Degree Global Forecast Grids Historical Archive. https://doi.org/10.5065/D65D8PWK.

Needham, M. R., and D. A. Randall, 2021a: Linking atmospheric cloud radiative effects and tropical precipitation. *Geophys Res Lett*, **48**, e2021GL094004, https://doi.org/10.1029/2021GL094004.

——, and ——, 2021b: Riehl and Malkus Revisited: The role of cloud radiative effects. *Journal of Geophysical Research: Atmospheres*, **126**, e2021JD035019, https://doi.org/10.1029/2021JD035019.

Rios-Berrios, R., 2020: Impacts of radiation and cold pools on the intensity and vortex tilt of weak tropical cyclones interacting with vertical wind shear. *J Atmos Sci*, **77**, 669–689, https://doi.org/10.1175/JAS-D-19-0159.1.

——, C. A. Davis, and R. D. Torn, 2018: A hypothesis for the intensification of tropical cyclones under moderate vertical wind shear. *J Atmos Sci*, **75**, 4149–4173, https://doi.org/10.1175/JAS-D-18-0070.1.

Rogers, R., 2010: Convective-scale structure and evolution during a high-resolution simulation of tropical cyclone rapid intensification. *J Atmos Sci*, **67**, 44–70, https://doi.org/10.1175/2009JAS3122.1.

Ruppert, J. H., A. A. Wing, X. Tang, and E. L. Duran, 2020: The critical role of cloud–infrared radiation feedback in tropical cyclone development. *Proceedings of the National Academy of Sciences*, **117**, 27884–27892, https://doi.org/10.1073/pnas.2013584117.

Skamarock, W. C., and Coauthors, 2008: A description of the advanced research WRF Version 3. https://doi.org/10.5065/D68S4MVH.

Steiner, M., R. A. Houze, and S. E. Yuter, 1995: Climatological characterization of three-dimensional storm structure from operational radar and rain gauge data. *Journal of Applied Meteorology*, **34**, 1978–2007, https://doi.org/10.1175/1520-0450(1995)034<1978:CCOTDS>2.0.CO;2.

Sui, C. H., and X. Li, 2005: A tendency of cloud ratio associated with the development of tropical water and ice clouds. *Terrestrial, Atmospheric and Oceanic Sciences*, **16**, 419–434, https://doi.org/10.3319/TAO.2005.16.2.419(A).

——, C. T. Tsay, and X. Li, 2007: Convective-stratiform rainfall separation by cloud content. *Journal of Geophysical Research Atmospheres*, **112**, https://doi.org/10.1029/2006JD008082.

Tang, B., and K. Emanuel, 2010: Midlevel ventilation's constraint on tropical cyclone intensity. *J Atmos Sci*, **67**, 1817–1830, https://doi.org/10.1175/2010JAS3318.1.

—, and —, 2012: A ventilation index for tropical cyclones. *Bull Am Meteorol Soc*, **93**, 1901–1912, https://doi.org/10.1175/BAMS-D-11-00165.1.

Tao, C., H. Jiang, and J. Zawislak, 2017: The relative importance of stratiform and convective rainfall in rapidly intensifying tropical cyclones. *Mon Weather Rev*, **145**, 795–809, https://doi.org/10.1175/MWR-D-16-0316.1.

Thompson, G., and T. Eidhammer, 2014: A study of aerosol impacts on clouds and precipitation development in a large winter cyclone. *J Atmos Sci*, **71**, 3636–3658, https://doi.org/10.1175/JAS-D-13-0305.1.

Voigt, A., N. Albern, P. Ceppi, K. Grise, Y. Li, and B. Medeiros, 2021: Clouds, radiation, and atmospheric circulation in the present-day climate and under climate change. *Wiley Interdiscip Rev Clim Change*, **12**, https://doi.org/10.1002/WCC.694.

Wall, C. J., J. R. Norris, B. Gasparini, W. L. Smith, M. M. Thieman, and O. Sourdeval, 2020: Observational evidence that radiative heating modifies the life cycle of tropical anvil clouds. *J Clim*, **33**, 8621–8640, https://doi.org/10.1175/JCLI-D-20-0204.1.

Wang, Z., 2012: Thermodynamic aspects of tropical cyclone formation. *J Atmos Sci*, **69**, 2433–2451, https://doi.org/10.1175/JAS-D-11-0298.1.

Wing, A. A., and K. A. Emanuel, 2014: Physical mechanisms controlling self-aggregation of convection in idealized numerical modeling simulations. *J Adv Model Earth Syst*, **6**, 59–74, https://doi.org/10.1002/2013MS000269.

—, and T. W. Cronin, 2016: Self-aggregation of convection in long channel geometry. *Quarterly Journal of the Royal Meteorological Society*, **142**, 1–15, https://doi.org/10.1002/QJ.2628.

—, S. J. Camargo, and A. H. Sobel, 2016: Role of radiative–convective feedbacks in spontaneous tropical cyclogenesis in idealized numerical simulations. *J Atmos Sci*, **73**, 2633–2642, https://doi.org/10.1175/JAS-D-15-0380.1.

—, K. Emanuel, C. E. Holloway, and C. Muller, 2017: Convective self-aggregation in numerical simulations: A review. 1–25, https://doi.org/10.1007/978-3-319-77273-8_1.

Wu, S. -N., B. J. Soden, and D. S. Nolan, 2021: Examining the role of cloud radiative interactions in tropical cyclone development using satellite measurements and WRF simulations. *Geophys Res Lett*, **48**, e2021GL093259, https://doi.org/10.1029/2021GL093259.

Yang, B., J. Nie, and Z. Tan, 2021: Radiation feedback accelerates the formation of Typhoon Haiyan (2013): The critical role of mid-level circulation. *Geophys Res Lett*, **48**, e2021GL094168, https://doi.org/10.1029/2021GL094168.

Yokoyama, C., and Y. N. Takayabu, 2008: A statistical study on rain characteristics of tropical cyclones using TRMM satellite data. *Mon Weather Rev*, **136**, 3848–3862, https://doi.org/10.1175/2008MWR2408.1.

Zelinka, M. D., T. A. Myers, D. T. McCoy, S. Po-Chedley, P. M. Caldwell, P. Ceppi, S. A. Klein, and K. E. Taylor, 2020: Causes of higher climate sensitivity in CMIP6 models. *Geophys Res Lett*, **47**, e2019GL085782, https://doi.org/10.1029/2019GL085782.